

Explainable Equivariant Neural Networks for Particle Physics: PELICAN

Alexander Bogatskiy^b Timothy Hoffman^a David W. Miller^{a,c} Jan T. Offermann^a Xiaoyang Liu^a

^a*Department of Physics, University of Chicago, Chicago, IL, U.S.A.*

^b*Center for Computational Mathematics, Flatiron Institute, New York, NY, U.S.A.*

^c*Enrico Fermi Institute, Chicago, IL, U.S.A.*

E-mail: abogatskiy@flatironinstitute.org, hoffmant@uchicago.edu,
jano@uchicago.edu

ABSTRACT: We present a comprehensive study of the PELICAN machine learning algorithm architecture in the context of both tagging (classification) and reconstructing (regression) Lorentz-boosted top quarks, including the difficult task of specifically identifying and measuring the W -boson inside the dense environment of the boosted hadronic final state. PELICAN is a novel permutation equivariant and Lorentz invariant or covariant aggregator network designed to overcome common limitations found in architectures applied to particle physics problems. Compared to many approaches that use non-specialized architectures that neglect underlying physics principles and require very large numbers of parameters, PELICAN employs a fundamentally symmetry group-based architecture that demonstrates benefits in terms of reduced complexity, increased interpretability, and raw performance. When tested on the standard task of Lorentz-boosted top quark tagging, PELICAN outperforms existing competitors with much lower model complexity and high sample efficiency. On the less common and more complex task of 4-momentum regression, PELICAN also outperforms hand-crafted, non-machine learning algorithms. We discuss the implications of symmetry-restricted architectures for the wider field of machine learning for physics.

Contents

1	Introduction	1
2	Equivariance and jet physics	3
3	PELICAN architecture	7
4	Tagging jets from Lorentz boosted top quarks	9
5	W-boson 4-momentum reconstruction	11
6	W-boson mass measurement	15
7	PELICAN explainability	19
8	IRC-safety and PELICAN	24
9	Conclusion	26
10	Acknowledgements	27
A	Additional results and plots	29
B	IRC-safety and Lorentz symmetry	31

1 Introduction

Identifying, reconstructing, and measuring the properties and dynamics of high-energy, short-distance particle phenomena is inherently an inference task, since direct access to the fundamental processes is often impossible due to the time and length scales at which they occur. The suite of detection techniques, pattern recognition algorithms, and measurement approaches used to perform this task inevitably imposes constraints on both the nature of the information used as well as on the form and structure of the results. Such constraints play a crucial role in the context of jet substructure measurements, in which detailed analysis is performed on the long-distance features of Lorentz-boosted particle decays, parton showering, and radiation patterns found in the collimated sprays of particles that form the jets themselves. In this work, we present a comprehensive analysis of a new approach to multiple jet substructure-based inference tasks using a machine learning (ML) architecture that fundamentally respects permutation and Lorentz-group symmetries: PELICAN, the permutation equivariant and Lorentz invariant or covariant aggregator network. Our approach thus imposes explicit physics-informed constraints on the system and consequently yields new insights and capabilities.

Decades of jet substructure research have yielded a wide range of approaches to performing inference tasks such as: distinguishing quark-initiated from gluon-initiated jets [1–5]; discriminating jets formed from Lorentz-boosted top quarks, Higgs and W -bosons, from the continuum background of jets formed from light-quarks and gluons [6–9]; dissecting and measuring the parton-shower structure of light-quark and gluon jets themselves [10–15]. Many approaches have been adopted to perform these tasks, including the direct use of discriminating high-level observables and multi-variate methods [16–18], as well as a growing number of ML architectures using a variety of latent-space representations. For a comprehensive overview of jet substructure measurements, see Refs. [19, 20], as well as Ref. [21] for a general review of ML methods in high-energy physics (including substructure measurements). As the model complexity has grown, so too

have questions regarding the relationship of both the methods and the constraints that they impose to the fundamental physical processes that they are used to model. In particular, the use of observables, architectures, and latent space representations that adhere closely to the structure and dynamics of the physics processes under study have been found to provide not only enhanced performance, but also significant insights and improvements in interpreting the results [18, 22, 23]. Imbuing these models with knowledge of, or even fundamental respect for, the symmetry group structures of the system under study has thus become increasingly impactful in the study of jet substructure, especially in the context of ML models and various neural network (NN) architectures [24–26].

There are several common approaches to enforcing continuous symmetries in NNs. Data augmentation can be used to train a model to have a particular sparsity structure and become approximately symmetric. However, when model complexity and interpretability are of concern, as is the case in particle physics and jet substructure analyses, a different approach is helpful. Similar issues arise with approaches that use preprocessing/normalization, which moreover come with inherent ambiguities and discontinuities that can be detrimental for sufficiently complex tasks.

Traditionally, ML algorithms are evaluated based on basic performance metrics such as accuracy and computational cost. However, in contexts where the trained algorithms are treated not only as predictors or generators, but as actual models for some process, – which is especially true in scientific applications – other metrics of model quality are valuable. Model complexity (defined as e.g. the number of parameters), explainability and interpretability can be important for making a viable physics model out of an ML algorithm. Further, certain problem-specific properties such as symmetries can be critical as well. Symmetries in ML are known to produce less complex models which respect basic geometrical rules and arguably provide more opportunities for interpretability and explainability (e.g. convolutional neural network (CNN) kernels are often interpreted as visual features). Even in realistic settings where the symmetries are merely approximate, symmetry-constrained architectures often outperform more general architectures in terms of pure accuracy (see e.g. Section 4), but even in cases when that is not true symmetric architectures should not be discounted due to their other benefits. For these reasons, as advocated for in Ref. [27], we have adopted an approach of building all symmetries directly into the PELICAN network architecture itself, similar to the inherent translational symmetry of CNNs.

Summary of results

In Section 2 we discuss equivariance in jet physics and introduce the tools we need to build an efficient equivariant architecture. In Section 3 we describe the architectures of PELICAN classifiers and regressors. Now we briefly summarize the main results presented in this work, corresponding to Sections 4 through 8.

Top-tagging with a PELICAN classifier We train PELICAN top taggers using a public benchmark dataset, to distinguish between top quark jets, and light quark and gluon jets. These taggers achieve state-of-the-art performance on the benchmark with fewer learnable parameters than the previous highest-performing network. PELICAN top taggers with as few as 11k parameters outperform all non-equivariant networks in the benchmark. See Section 4 for details.

W-boson 4-momentum reconstruction with PELICAN We train a PELICAN model using a custom dataset [28] of fully-hadronic top decays to reconstruct the full 4-momentum of the intermediate W -bosons. Specifically, PELICAN uses 4-momenta of the top quark jet constituents as inputs. PELICAN performs favorably in reconstructing the full W momentum when compared with the Johns Hopkins (JH) top tagger [7], which produces W candidates for the subset of jets that pass its tagging. PELICAN achieves better p_T , mass, and angular resolutions on JH top-tagged jets – and achieves comparable resolutions to the JH tagger even when evaluated on the full dataset. Additionally, we train a PELICAN model to reconstruct the 4-momentum of only the products of the $W \rightarrow qq'$ decay which are contained within the jet. We discuss differences in performance and effects of this choice in reconstruction targets in Section 5.

W-boson mass reconstruction with PELICAN Mass reconstruction is a common particle physics analysis task, and any reconstruction algorithm should be robust and relatively free of bias. In Section 6 we discuss the nuances of PELICAN mass reconstruction targeting the W -bosons in the above-mentioned dataset [28] as an example. The results show that eliminating bias in the underlying dataset is required to produce an unbiased

final algorithm. In the case of W mass reconstruction, this is achieved by training PELICAN on a dataset with multiple values of m_W .

Explaining PELICAN weights PELICAN’s respect of the particle permutation and Lorentz symmetries inherent to particle datasets provides it with explainability and interpretability rarely found in particle physics machine learning applications. In Section 7 we investigate the rich penultimate layer of PELICAN and its discriminatory power. In particular, we discuss interpretations of PELICAN as a soft clustering and detector-unfolding algorithm of sorts.

IRC-safety and PELICAN In particle physics, IRC-safety is an algorithmic concern which restricts tools to be robust with respect to soft-particle emissions (infrared – IR) and collinear (C) splits due to divergences in perturbative quantum chromodynamics (QCD). In Section 8 we modify PELICAN into IR-safe and IRC-safe versions and discuss their relative performances.

2 Equivariance and jet physics

This section aims to establish a clear connection between the group theory that underlies the PELICAN architecture and the implementation of this approach for both classification and regression, as described in Section 3.

Given a symmetry group G and two sets X, Y on which an action of G is defined, a mapping $F : X \rightarrow Y$ is called *G-equivariant* if $F(g \cdot x) = g \cdot F(x)$ for any $x \in X$ and $g \in G$. In particular, if the action of G on Y happens to be trivial (i.e. $g \cdot y = y$ for all g, y), then F is called *invariant*. In relativistic physics, equivariant maps are typically represented by tensors with equivariant spacetime indices treated via Einstein notation. For instance, the electromagnetic field tensor $F^{\mu\nu}$ can be viewed as a Lorentz-equivariant mapping from covariant vector fields to contravariant ones. In this work we will be interested in tasks from jet physics that can be reduced to learning a Lorentz-equivariant map. In this section we review some basics of the Lorentz symmetry in the context of such tasks.

2.1 Lorentz symmetry and jets

Lorentz symmetry is one of the fundamental symmetries of the Standard Model of particle physics. The full Lorentz group $O(1, 3)$ can be defined as the set of linear transformations of the 4-dimensional spacetime that preserve the Minkowski metric $\eta = \text{diag}(1, -1, -1, -1)$. However, in this work we will restrict ourselves to the *proper orthochronous* subgroup $SO^+(1, 3)$ that preserves spatial and temporal orientations. Lorentz invariance is the mathematical encapsulation of the fact that the outcomes of physical phenomena don’t depend on the inertial frame of the observer. In the context of particle accelerators, this boils down to the observation that all initial and final states of a particle interaction are the same in all inertial frames. This is formally reflected in the fact that the Standard Model of particle physics is Lorentz-invariant, and therefore any model of any physically relevant processes encompassed by the Standard Model can be as well.

A couple subtle points are worth addressing before applying Lorentz symmetry to experimental tasks in jet physics. Neither the actual particle detectors nor the software simulating particle decays and their detection are Lorentz-invariant. Reasons for this include: non-invariant corrections to perturbative computations in quantum chromodynamics (QCD); non-invariance of jet clustering algorithms; practical limitations of detectors such as finite resolution and energy cutoffs. Nevertheless, it is still valid to learn Lorentz-invariant models from data obtained this way. Firstly, QCD is globally Lorentz-invariant and boosting the *entire* event does not change the outcome of the decay process. As long as inference is performed on data obtained in conditions similar to the conditions of the perturbative simulation, corrections from such effects as the running of the couplings with varying momentum scales are not a concern either. The same applies to jet clustering algorithms and the finite detection resolution: as long as the data used for inference was obtained in the same reference frame as the data used for training, the inference is valid and the outputs are expected to be Lorentz-equivariant. Finally, the fact that the detector itself introduces a fixed reference frame can be fully addressed without breaking the symmetry of the model by including detector geometry among its inputs. This will be discussed below in Section 3.1.

2.2 Lorentz invariance

The classification task considered in this work is exactly Lorentz invariant. The physical content of this statement will be discussed below, but mathematically it simply means the following. If the inputs to the network are a collection of 4-vectors (energy-momentum vectors in our case) p_1, \dots, p_N , the output is $F(p_1, \dots, p_N)$, and $\Lambda \in \text{SO}^+(1, 3)$ is a Lorentz transformation, then

$$F(\Lambda p_1, \dots, \Lambda p_N) = F(p_1, \dots, p_N). \quad (2.1)$$

There are a few ways of constructing a machine learning model that satisfies a constraint of this kind. The simplest one is to hand-pick a set of invariant observables (such as particle masses, relative masses, particle identification labels and charge) and feed them into a generic neural network architecture.

Another approach inspired by convolutional networks is to preserve group-equivariant latent representations in the hidden layers. In this case the neuron nonlinearity must be a Lorentz-equivariant operation, and examples of this can be found in both the Lorentz Group Network (LGN) [25] and LorentzNet [26]. As in traditional CNN's used in image processing, equivariant latent representations, as opposed to invariant ones, can regularize the network via efficient weight-sharing and improve training.

Here, we take a slightly different approach. Given a set of 4-vector inputs p_1, \dots, p_N , we compute a *complete* set of Lorentz invariants on that set. For classical groups, including the Lorentz group, the space of invariants constructed out of a collection of vectors in the fundamental representation are functions of only the pairwise invariant dot products (using the appropriate invariant quadratic form for the given symmetry group) and of square determinants (of, say, 4 column-vectors for the Lorentz group) [29]. Furthermore, if the invariant is required to be symmetric in the vector inputs, then it's *only* a function of the dot products (see also the discussion in Ref. [30]). In short, all totally symmetric Lorentz invariants can be written in the following form:

$$I(p_1, \dots, p_N) = f(\{p_i \cdot p_j\}_{i,j}). \quad (2.2)$$

This is the first key idea used in our architecture. The first step performed by the input layer is the computation of the $N \times N$ array of dot products between the particle 4-momenta (also known as the Gram matrix). Note, however, that from simple dimension counting it's clear that the $N(N-1)/2$ components of the Gram matrix $\{p_i \cdot p_j\}$ can't be independent. The physical manifold inside this high-dimensional space is defined by the set of constraints $\det M_5 = 0$ for *every* 5-minor M_5 of the Gram matrix (that is, any matrix obtained from the original one by crossing out $N-5$ rows and $N-5$ columns). Moreover, a causally related set of points such as a particle jet will always satisfy $p_i \cdot p_j \geq 0$ for all i, j . Therefore a neural network whose input is an $N \times N$ matrix will learn the task only on this $(4N-6)$ -dimensional submanifold of \mathbb{R}^{N^2} . The outputs of the trained model on the rest of the space will be uncontrollable and physically meaningless.

2.3 Permutation equivariance

Particle data are often interpreted as a point cloud since there is no natural ordering on the vectors. For such problems it makes sense to use one of the permutation-invariant or equivariant architectures. One of the simplest approaches is called Deep Sets [31], which has been applied to jet tagging [24] and even heavy-flavor tagging [32]. The fundamental fact used in deep sets is that any permutation-invariant continuous mapping of inputs x_1, \dots, x_N can be written in the form $\psi(\sum_i \varphi(x_i))$, where ψ and φ can be approximated by neural networks.

The main limitation of permutation-invariant architectures such as Deep Sets is the difficulty of training. Since aggregation (summation over the particle index) happens only once, the Deep Sets architecture can struggle with modeling complex higher-order interactions between the particles [33]. The network representing ψ is forced to be a relatively wide fully connected network, which makes it difficult to train.

The alternative to permutation-invariant architectures is provided by permutation-*equivariant* ones. Given a symmetry group G (e.g. the group of permutations), a representation (V, ρ) is a tuple where V is a set and $\rho : G \times V \rightarrow V$ is a map that becomes a bijection $\rho_g = \rho(g, \cdot) : V \rightarrow V$ for any fixed value of the first argument, $\rho_e = \text{id}$, and $\rho_{g^{-1}} = \rho_g^{-1}$. Given two representations (V, ρ) and (V', ρ') of a group G , a map $F : V \rightarrow V'$ is called equivariant if it *intertwines* the two representations, that is:

$$F(\rho_g(v)) = \rho'_g(F(v)), \quad v \in V, g \in G. \quad (2.3)$$

Equivariance is a key property of all convolutional networks – for example, in CNN’s the convolution operation is inherently equivariant with respect to translations (up to edge effects).

Similarly, Graph Neural Networks (GNN’s) use permutation equivariance to force architectures that respect the underlying graph structure and don’t exhibit false implicit biases that produce different outputs after a mere renaming of the graph vertices. In this context, we review the standard definition of a message passing layer where the particles are treated as nodes in a graph (for example, the fully connected graph), and every layer of the network only updates the activation at every node. If we denote by f_i the data assigned to node i , then the message passing layer will typically construct “messages” $m_{ij} = m(f_i, f_j)$ and then update each node by aggregating the messages coming from all neighbors of that node and combining the result with the original state of the node: $f'_i = \psi(f_i, \sum_j m_{ji})$. Sometimes the graph also possesses “edge data” D_{ij} that can be incorporated into the message-forming stage.

Message passing architectures have been successfully applied to jet tagging, most prominently in Refs. [25, 26]. However, attempts to combine message passing with Lorentz invariance runs into a major obstacle: as we have seen, the inputs to the network consist of *nothing but* edge data $d_{ij} = p_i \cdot p_j$. Traditional message passing would require a reduction of this set of inputs to a point cloud (with only one particle index), potentially restricting the set of possible higher-order interactions between the points. To avoid making these unnecessary choices, we employ the general permutation-equivariant layers suggested in Refs. [34, 35].

In the general setting, permutation equivariance is a constraint on mappings F between arrays $T_{i_1 i_2 \dots i_r}$ of any rank r , every index $i_k \in \{1, \dots, N\}$ referring to a particle label, whereby permutations of the particles “commute” with the map:

$$F(\pi \circ T_{i_1 i_2 \dots i_r}) = \pi \circ F(T_{i_1 i_2 \dots i_r}), \quad \pi \in S_N. \quad (2.4)$$

Here, the action of permutations is “diagonal”: $\pi \circ T_{i_1 i_2 \dots i_r} = T_{\pi(i_1) \dots \pi(i_r)}$. Graph Neural Networks explicitly implement this constraint for rank 1 arrays (node information). A higher-order generalization of the Message Passing layer can be defined as

$$\textbf{Equivariant Layer: } T^{(\ell+1)} = \text{AGG} \circ \text{MSG}(T^{(\ell)}). \quad (2.5)$$

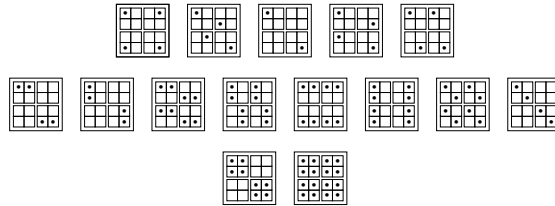
Here, MSG is a node-wise nonlinear map (“message forming”) shared between all nodes, and AGG is a general permutation-equivariant linear mapping (“aggregation”) acting on the particle indices of T . Note that whether MSG is node-wise and whether AGG is linear is somewhat ambiguous based on how one separates the mappings into their components, which is why, in particular, the traditional formulation of message passing allows messages to be functions of pairs of nodes. In practice, our aggregation block will also involve a nonlinear activation function.

2.4 Elementary equivariant aggregators

It only remains to describe the exact structure of the equivariant aggregation layers defined above. Since the general case is presented in Refs. [34, 35], here we will only present the layers that we need for jet tagging. Since the input is an array of rank 2, the main equivariant layer for us is one that transforms arrays of rank 2 to other arrays of the same rank: $T_{ij} \mapsto T'_{ij}$. The space of all linear maps of this type turns out to be 15-dimensional. The basis elements of this space can be conveniently illustrated using binary arrays of rank 4. There are 15 such arrays B^a_{ijkl} , $a = 1, \dots, 15$, and the action of the equivariant layer can be written as

$$T'^a_{ij} = \sum_{k,l=1}^N B^a_{ijkl} T_{kl}. \quad (2.6)$$

The 15 aggregators B^a are easy to visualize. This is done below for $N = 2$.



The smallest squares represent components of the input 2×2 array, and the larger 2×2 squares represent components of the output array. Dots represent the non-zero components of the binary tensors B^a , and every component of the output tensor is the result of aggregation over all inputs marked by the dots. Output components that lack any dots are set to be a fixed constant, by default zero (the affine versions of these mappings include two such parameters: one constant for the diagonal and another for the remaining components). By “aggregation” we mean, in general, any symmetric function, but in practice it is usually a sum or mean. For example, the first aggregator is simply the identity map on matrices: the ij ’th component of the output array is the result of aggregation over only the ij ’th component of the input. The second aggregator realizes the transposition of arrays $T'_{ij} = T_{ji}$. The following three aggregators represent various ways of embedding the diagonal of the input array in an equivariant way. It is easy to see that simultaneously swapping the two rows and the two columns of the input is equivalent to doing the same to the output, which confirms equivariance. These first 5 aggregators are “order zero” in N because they do not actually perform any aggregation. Instead, they can be thought of as permutation-equivariant skip-connections.

The second group of 8 “order one” aggregators aggregate over N components of the input by aggregating either over rows, columns, or the diagonal, and then embedding the result into the output array in all possible equivariant ways. Finally, the last 2 aggregators are the “order two” aggregators that aggregate over all N^2 components of the input.

If we allow aggregators to be nonlinear, then they can take the following form: the binary array B^a selects a subset of the components of the input array, and then a general symmetric function S^a is applied to that subset:

$$T'_{ij}{}^a = S^a \left(\{T_{kl} \mid k, l : B^a_{ijkl} \neq 0\} \right). \quad (2.7)$$

In practice we define S^a as the mean of its inputs followed by an additional scaling by a factor of $N^{\alpha_a} / \bar{N}^{\alpha_a}$ with learnable exponents α_a , where \bar{N} is a constant representing the typical number of input vectors expected in the dataset, provided to the model as a hyperparameter.

2.5 Equivariance and Jet Physics

There are several reasons for enforcing the full Lorentz symmetry in our ML models. First and foremost, it is a fundamental symmetry of the space to which the inputs belong. Lorentz transformations represent the effect of switching between different inertial frames, and most fundamental processes in physics are independent of the choice of the observer’s inertial frame: if a given collection of particles consists of products of a decay of a top quark for one observer, then the same is true for all other observers.

Nevertheless, some processes involved in generating and observing high-energy collision events break the Lorentz symmetry in some subtle ways. At the fundamental level, the running of the couplings in QCD can cause Lorentz symmetry breaking in the parton shower distribution functions. Even the amount of final decay products depends on the transversal boost of the initial parton-level particles. However, there is no question that both the original protons and the final (asymptotic) decay products are accurately represented by a collection of 4-vectors subject to the spacetime Lorentz symmetry: the asymptotic outcome of a collision event is independent of the observer’s reference frame.

Another reason for symmetry-restricted modeling is that, from the geometric perspective, only some mathematical operations are permissible when working with objects that transform in a certain way under a symmetry group. A non-equivariant neural network effectively neglects the vector nature of the inputs by treating individual components of the input vectors as scalars. While improving network expressivity, non-equivariance fails to deliver physically interpretable models. Ultimately, a statement about equivariance is a statement about what the basic *features* of the data are – e.g. vectors are features, but the individual components of those vectors are not.

More relevant to the applications is the fact that both the simulation and the observation of collisions inevitably involves some degree of *clustering*. A particle detector is made of cells (e.g. calorimeters) of finite size and as such is unable to distinguish between some particles that are collinear or very close to collinear. Similarly, the standard algorithms for collision simulation typically perform *jet clustering* to closely reproduce the detector behavior. Clustering of course is not a Lorentz-invariant procedure: particle tracks that diverge by a small angle in one frame will diverge by a large angle in another highly boosted frame. However, this limitation of Lorentz-invariant architectures is fairly minor. Since clustering is always done in a fixed

laboratory frame, it is still reasonable to impose the full Lorentz symmetry on the resulting 4-vector data. So unless the pre-clustering data itself is coming from multiple significantly different inertial frames, clustering is not interfering with the fundamental symmetry. Simply put, however a given set of 4-vectors is obtained and represented in a specific inertial frame, those vectors will respect the Lorentz symmetry.

3 PELICAN architecture

The PELICAN architecture is simplified with respect to LGN due to the use of the complete set of dot products between the input 4-momenta (See Section 2), and this has significant implications for both the overall architecture as well as the ease of training and interpretability of the network. This section discusses each of the primary components of the network, including the inputs and their embedding, the permutation and Lorentz equivariant blocks, and the output layers that determine the structure of the result, namely classification or 4-vector regression.

3.1 Inputs and embeddings

Dot Products and Beams On the input side of the architecture, the first step is to compute all pairwise dot products of the input 4-momenta. Appended to the list of these 4-momenta are two auxiliary beam particles with 4-momenta $(1, 0, 0, \pm 1)$. This is helpful since the datasets we are using are all simulated in a fixed laboratory frame where the original proton-proton collision happens along the z -axis, and the auxiliary inputs restore this orientational knowledge. In particular, the dot products between constituents and beams give PELICAN access to the energies and transverse momenta of all constituents.

It is worth emphasizing that introducing beams in this manner allows us to fix a particular spatial orientation of the events without restricting or violating the global Lorentz symmetry inherent in the architecture. Indeed, if one were to treat the auxiliary beams as constant vectors of hyperparameters, then this action would reduce the full Lorentz symmetry to merely rotations in the xy -plane and z -boosts. However, due to the fact that the beams are fed into the network on equal footing with all other inputs, they are properly treated as full-fledged 4-vectors that should also transform under the global Lorentz symmetry. Thus, counter-intuitively, we let the network access individual energies, transverse momenta and z -momenta while still preserving full Lorentz symmetry and all the computational benefits that come with it.

Input Embedding Next there is an embedding layer that applies the function $f_\alpha(x) = ((1+x)^\alpha - 1)/\alpha$ to each dot product with $C^0 - 2$ different values of the trainable parameter α (initialized to span the interval $[0.05, 0.5]$). Then the result goes through a masked BatchNorm2D layer. Finally, this array of scalars gets concatenated with two labels L_i, L_j per dot product $d_{ij} = p_i \cdot p_j$ that indicate whether each of particles i and j is a beam or not. The label for a beam is chosen to be 1 and the label for all other particles is 0. At the end of this input block, we have a tensor of shape $[B, N_{\max}, N_{\max}, C^0]$ where the feature vector for each particle pair has the form $\left(\text{BatchNorm2D}\left(f_{\alpha_1}(d_{ij}), \dots, f_{\alpha_{C^0-2}}(d_{ij})\right), L_i, L_j\right)$.

3.2 Permutation equivariant blocks

The main element of the equivariant architecture is the permutation-equivariant block transforming arrays of rank 2. Namely, we assume that the input tensor to the block has shape $[B, N_{\max}, N_{\max}, C^l]$, where B is the batch size, N_{\max} is the maximum number of jet constituents per event (with zero padding for events with fewer constituents), and C^l is the number of input channels. We also use a binary mask of shape $[B, N_{\max}, N_{\max}]$ to appropriately exclude the zero padding from operations like BatchNorm and aggregation. The output of the block will be a similar tensor of shape $[B, N_{\max}, N_{\max}, C^{l+1}]$ with the same mask.

As outlined above, the equivariant layer consists of a message block and an aggregation block. The message block is chosen to be a dense multilayer perceptron (MLP) acting on the channel dimension with a LeakyReLU activation and BatchNorm2D (normalization over the first three dimensions of the tensor, for each channel separately, followed by an affine transform with two learnable parameters per channel). Here we use a masked implementation of batch normalization so that the variable particle number is respected. The message block is then followed by Dropout that zeroes out each of the $B \times N_{\max}^2 \times C_{\text{eq}}^l$ components independently with a certain probability.

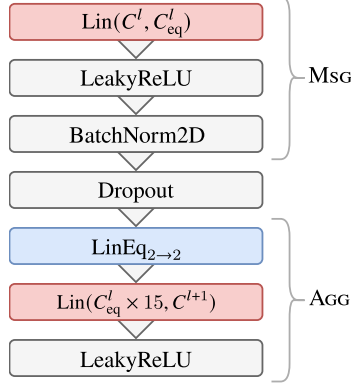


Figure 1: The PELICAN equivariant block updating square arrays.

The aggregation block applies 15 linear aggregation functions ($\text{LinEq}_{2 \rightarrow 2}$) which, for each component of the output tensor, compute the mean over some subset of the components of the input tensor, as explained in Section 2.4. Note that this is a non-parametric transformation performed on each channel separately. Each of the $C_{\text{eq}}^l \times 15$ resulting aggregation values is then independently multiplied by $N^\alpha / \bar{N}^\alpha$ with a trainable exponent α (initialized as a random float in $[0, 1]$), where N is the number of particles in the corresponding event. This allows for some flexibility in the aggregation process, for example $\alpha = 1$ returns the sum aggregation function, and combining multiple aggregators is known to boost accuracy [34].

Aggregation is followed by a dense layer that mixes the $C_{\text{eq}}^l \times 15$ aggregators down to C^{l+1} features. Due to the size of this layer, we employ a simple factorization to reduce the number of parameters. Namely the weight tensor W_{abc} , where a is the input channel index, b is the basis index (1 to 15), and c is the output channel index, can be replaced by the following combination:

$$W_{abc} = W_{ab}^0 W_{ac}^1 + W_{cb}^2 W_{ac}^3. \quad (3.1)$$

Here, the first term first mixes the 15 aggregators among each other for each output channel, and then mixes the channels. Similarly, the second term first mixes the 15 aggregators for each input channel, and then mixes the channels.

The final result is a tensor of shape $[B, N_{\text{max}}, N_{\text{max}}, C^{l+1}]$, so these equivariant layers can be stacked multiple times.

3.3 Classification and 4-vector regression outputs

One of the strengths of the PELICAN architecture is the ability to easily switch between serving as a classification tool for discriminating between Lorentz-boosted top quarks and the QCD background, to being able to provide 4-vector regression results, such as momentum reconstruction.

PELICAN classifier To build a classifier, aside from the $\text{Eq}_{2 \rightarrow 2}$ equivariant layer one needs a $\text{Eq}_{2 \rightarrow 0}$ layer that reduces the rank 2 array to permutation-invariant scalars. This layer involves just 2 aggregation functions instead of 15 – the trace and the total sum of the input square matrix, but is otherwise identical to the equivariant layer described in the last section.

$$\{d_{ij}\} \rightarrow \boxed{\text{Emb} \rightarrow [\text{Eq}_{2 \rightarrow 2}]^L \rightarrow \text{Eq}_{2 \rightarrow 0} \rightarrow \text{MLP}} \rightarrow \{w_c\} \quad (3.2)$$

From the input block, the tensor is passed through L equivariant $\text{Eq}_{2 \rightarrow 2}$ layers, and the $\text{Eq}_{2 \rightarrow 0}$ layer with dropout. This produces a tensor of shape $[B, C_{\text{out}}]$. One final MLP mixes this down to just 2 classification weights per event. A cross-entropy loss function is then used for optimization.

PELICAN 4-vector regression The same architecture can also be easily adapted for 4-vector regression tasks, such as momentum reconstruction. Any Lorentz-equivariant map from a collection of 4-vectors

p_1, \dots, p_N to one (or several) 4-vector has the form

$$F(p_1, \dots, p_N) = \sum_{i=1}^N f_i(p_1, \dots, p_N) \cdot p_i, \quad (3.3)$$

where f_i 's are Lorentz-invariant functions [36]. Combining this with permutation invariance, we conclude that the multi-valued map $(p_1, \dots, p_N) \mapsto (f_1, \dots, f_N)$ must also be equivariant with respect to the permutations of the inputs.

The only change required to the architecture we've introduced for classification is that $\text{Eq}_{2 \rightarrow 0}$ must be replaced with $\text{Eq}_{2 \rightarrow 1}$ and the final output layer must have only one output channel (assuming we are regressing on a single 4-vector). The $\text{Eq}_{2 \rightarrow 1}$ layer is again identical to $\text{Eq}_{2 \rightarrow 2}$ except that it uses only 4 linear aggregators: row sums, column sums, trace, and full sum. The architecture is summarized by the following diagram, where we treat d_{ij} as the inputs and f_i as the outputs, keeping in mind formula (3.3) that lets us recover the final predicted vector.

$$\{d_{ij}\} \rightarrow \boxed{\text{Emb} \rightarrow [\text{Eq}_{2 \rightarrow 2}]^L \rightarrow \text{Eq}_{2 \rightarrow 1} \rightarrow \text{MLP}} \rightarrow \{f_i\}_{i=1}^N \quad (3.4)$$

4 Tagging jets from Lorentz boosted top quarks

This section presents the dataset, training approach, and results of using PELICAN as a classifier in the context of identifying Lorentz-boosted top quarks. Three different versions of PELICAN are discussed, each with a different size in terms both the width of the network and the number of trainable parameters. Lastly, the dependence of the performance on the size of the training dataset is also presented, providing a quantitative relationship between the size of the network, the training dataset efficiency, and the resulting performance.

4.1 Classification dataset

We perform top-tagging on the reference dataset [37], which was also used in Ref. [8]. This dataset consists of 2M entries, each entry corresponding with a single hadronic top jet or the leading jet from a QCD dijet event. There are 1.2M training entries, 400k validation entries and 400k testing entries. The events were generated with PYTHIA8, and the DELPHES framework [38] was used for fast detector simulation in order to incorporate detector effects. For each jet, the 4-momentum of the 200 leading constituents are stored in Cartesian coordinates (E, p_x, p_y, p_z) , in order of decreasing p_T . This list is zero-padded, and all jets in the dataset have fewer than 200 constituents. The dataset does not contain any other information on the jet constituents, such as charge or spin.

4.2 Classification training procedure

The top-tagging model contains five $\text{Eq}_{2 \rightarrow 2}$ blocks of identical shapes. We train three different versions of the model with different widths. The widest model has 132 input and 78 output channels on every messaging layer (the equivariant layer then produces 132×15 quantities which get mixed down to 78 channels by a fully connected linear layer). The output MLP is just one layer that mixes 132 channels down to 2 classification weights. The number of jet constituents was capped at 80 (no noticeable performance gain was seen beyond that number). The dropout rate was 0.025, and the model was optimized using the ADAMW optimizer [39] with weight decay of 0.005. The training on the full dataset went on for 35 epochs with the same learning rate schedule as in Ref. [26]: 4 epochs of linear warm-up up to learning rate of 0.001, followed by 28 epochs of COSINEANNEALINGLR with T_0 of 4 epochs and $T_{\text{mult}} = 2$, and then 3 epochs of exponentially decaying learning rate with exponent $\gamma = 0.5$ per epoch. The three models were trained on Nvidia H100 GPU's with batch size of 100, taking 0.43, 0.17, or 0.08 seconds per batch, respectively. Inference took 0.17, 0.07, or 0.04 seconds per batch. Batches were shuffled between epochs.

4.3 Classification results

Figure 2 shows the *receiver operating characteristic*, here represented by the background rejection as a function of the signal efficiency, for the classification performance. In Table 1 we compare the accuracy, area under the curve (AUC), and background rejection values at 30% signal efficiency between PELICAN

Architecture	Accuracy	AUC	$1/\epsilon_B$	# Params
TopoDNN[40]	0.916	0.972	382 ± 5	59k
LGN[25]	0.929(1)	0.964(14)	424 ± 82	4.5k
PFN[24]	0.932	0.982	891 ± 18	82k
ResNeXt[8]	0.936	0.984	1122 ± 47	1.46M
ParticleNet[41]	0.938	0.985	1298 ± 46	498k
LorentzNet[26]	0.942	0.9868	2195 ± 173	220k
PELICAN _{132/78}	0.9425(1)	0.9870(1)	2250 ± 75	208k
PELICAN _{60/35}	0.9423(1)	0.9868(1)	2133 ± 148	48k
PELICAN _{25/15}	0.9410(3)	0.9858(4)	1879 ± 103	11k

Table 1: Comparison of PELICAN models trained on different fractions of the training dataset. The subscripts indicate the width of the network: e.g. 132/78 means each Msg layer has 132 input and 78 output channels.

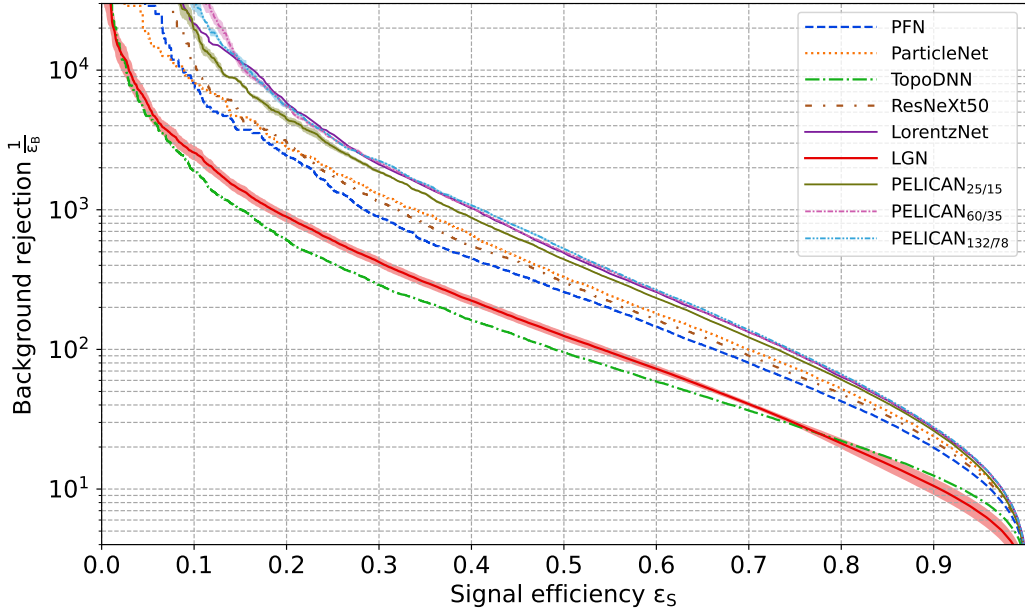


Figure 2: Performance of various machine learning architectures represented by the background rejection as a function of the signal efficiency.

and a multiple existing ML top-taggers, including the previous state-of-the-art LorentzNet [26]. We trained three PELICAN top-taggers with layers of differing widths, with 208k, 48k, and 11k trainable parameters respectively. The results are averaged over 5 random initialization seeds, and the uncertainties are given by the standard deviation. The large PELICAN model improves upon the LorentzNet result with a comparable number of parameters, and the medium model roughly matches LorentzNet despite having 5 times fewer parameters. Perhaps most remarkably, the small model with 11k parameters beats every pre-LorentzNet competitor despite having at least times fewer parameters, and up to 130 times fewer parameters, than other networks.

In addition to different model sizes, we also explore sample efficiency. Each of the three models above was trained on 0.5%, 1% and 5% of the training data and compared to the original. For these, the training went on for 70 epochs with 60 epochs of COSINEANNEALINGLR instead of 28, and 6 epochs of exponential decay instead of 3. The results can be found in Table 2. Notice that at lower amounts of training data the differences in performance between models of different width become much less significant, and at 1% and 0.5% of training data all three models fall within each other’s uncertainty ranges. These results suggest that the larger PELICAN networks are likely able to learn a greater range of more subtle features from the training data and thus benefit from seeing a larger training dataset. On the other hand, the primary features are already

learnable with just a few percent of the data. In particular, with 5% of the training data and only 11k learnable parameters, the PELICAN_{25/15} version of the network appears to achieve the similar background rejection performance as ResNeXt, which uses 1.46M parameters learning on the full dataset.

Model	% training data	Accuracy	AUC	$1/\epsilon_B$
PELICAN _{132/78}	100%	0.9425(1)	0.9870(1)	2250 ± 75
	5%	0.9366(3)	0.9841(1)	1213 ± 79
	1%	0.9316(6)	0.9810(5)	789 ± 49
	0.5%	0.9289(11)	0.9800(5)	633 ± 28
PELICAN _{60/35}	100%	0.9423(1)	0.9868(1)	2133 ± 148
	5%	0.9368(2)	0.9841(1)	1148 ± 49
	1%	0.9323(3)	0.9813(4)	799 ± 52
	0.5%	0.9289(9)	0.9795(5)	637 ± 105
PELICAN _{25/15}	100%	0.9410(3)	0.9858(4)	1879 ± 103
	5%	0.9361(5)	0.9835(2)	1122 ± 44
	1%	0.9316(1)	0.9810(5)	798 ± 116
	0.5%	0.9286(11)	0.9795(6)	615 ± 133

Table 2: Comparison of PELICAN models trained on different fractions of the training data.

5 W-boson 4-momentum reconstruction

To test the equivariant regression architecture described in Section 3 we chose a task where the aim is to reconstruct (or *predict*) the full 4-momentum of the W -boson within the Lorentz-boosted top quark decay products. Specifically, we consider the same hadronic top quark decay that constitutes the signal in the top-tagging dataset, which uses the $t \rightarrow bW \rightarrow bq\bar{q}$ two-step decay, followed by hadronization, showering, and detection. Our aim is to reconstruct the true 4-momentum of the W -boson given the full set of observed final state particles of the top decay, as represented by the jet constituents.

5.1 Regression dataset

The dataset used for the regression task consists of 1.5M $t\bar{t}$ events simulated with PYTHIA8, with 700k events for training, 200k events for validation, and 500k events for testing (with an additional 100k events set aside in a second testing set). From each event, we cluster anti- k_T jets with $R = 0.8$ using FASTJET [42] and we select the jet nearest to the truth-level top quark in (η, ϕ) , requiring the distance between the top quark and the jet to satisfy $\Delta R(\text{top quark, jet}) < 0.8$. This jet clustering is done both at truth-level, and using calorimeter tower objects produced by running the event through DELPHES fast detector simulation using the ATLAS detector card. Thus, each *event* in the dataset corresponds to a single jet, and includes information for truth-level particles such as the truth-level top quark – we may therefore use the terms *jet* and *event* interchangeably below with the understanding that each event in the dataset has one and only one jet recorded. This dataset is publicly available via Zenodo [28], where a full description of the various data fields is provided. Here we provide only an overview of some key features:

1. There are two versions of the dataset, corresponding with truth- and reconstruction-level (DELPHES) jets. The events are the same between versions, so the two can be compared event-by-event to study the effects of detector reconstruction on network training and performance.
2. The input data for the network are the 4-momenta of the 200 leading jet constituents. For use as possible regression targets and for defining jet containment (explained below), each event contains
 - (a) the truth-level top quark that initiated the jet,
 - (b) the bottom quark from top quark decay,
 - (c) the W -boson from top quark decay,
 - (d) the two quarks from subsequent W -boson decay ($W \rightarrow q\bar{q}'$),

In addition, the event contains the stable W -boson daughter particles. These are the truth-level, final state particles that are traced back to the W -boson by `PYTHIA`.

3. Each jet is tagged with the Johns Hopkins top tagger [7] (JH), as implemented in `FASTJET`. This allows us to define a subpopulation of JH-tagged events, which we shall sometimes refer to as *JH events*. For jets that it tags as top quark jets, JH provides a W -boson candidate constructed from subjets.
4. Each jet is also tagged as whether or not it is *fully-contained* (FC). We define FC events as those where the b -quark, as well as the two quarks from $W \rightarrow qq'$ decay, are within $\Delta R < 0.6$ of the jet centroid (i.e. within 75% of the jet radius). In such cases almost all of the W daughters are contained within the jet and we can expect a good reconstruction of the W momentum. FC events comprise 75% of the dataset.

5.2 Regression training procedure

Our model has 4 equivariant $\text{Eq}_{2 \rightarrow 2}$ blocks. Each messaging layer takes in 132 channels and outputs 78 channels. Conversely, each equivariant aggregation layer has 78 input channels and outputs 132 channels. The $\text{Eq}_{2 \rightarrow 1}$ block has the same shape, and the final fully connected layer has the shape 1×132 . There are 210k parameters in total. Assuming N non-zero input jet constituents, this produces N scalar coefficients c_i with zero-padding, which are the Lorentz invariants introduced in (3.3). The reconstructed 4-momentum is then computed via

$$p_{\text{reco}} = \sum_i c_i p_i. \quad (5.1)$$

The training regime for this task is essentially identical to the one for top-tagging: `ADAMW` optimizer with weight decay of 0.01, 35 epochs in total with 4 epochs of warm-up and exponential learning rate decay for the last 3 epochs. The main difference is in the choice of the loss function $L(p_{\text{reco}}, p_{\text{target}})$. Spacetime geometry allows for many choices of this function, which in turn will affect the shape of the landscape near p_{target} and in turn the precision of various reconstructed features of the vector, such as the mass, energy, spatial momentum, transverse momentum, and direction. It is even possible to construct Lorentz-invariant loss functions to make the training process itself equivariant. Nevertheless, for the purpose of simultaneous reconstruction of the direction and the mass of the W -boson, m_W , we found

$$L = 0.01 \|p_{\text{reco}} - p_{\text{target}}\| + 0.05 |m_{\text{reco}} - m_{\text{target}}| \quad (5.2)$$

to be very effective. It uses all 4 components of the target vector and strikes a good balance between the precision of the reconstructed mass and spatial momentum.

A rarely discussed feature of this task is the choice of the target vector p_{target} . Even though our ultimate inference target is the true W momentum p_{true}^W , it is not necessarily the best training target given the nature of the dataset. Detection and jet clustering include multiple energy, momentum, and spatial cuts that exclude some decay products from the final jet. For instance, one of the three quarks in $t \rightarrow bqq$ might fall outside of the $R = 0.8$ radius of the jet clustering algorithm, in which case most of the decay products of that quark are likely to be absent from the event record. If many of the decay products of the W -boson are missing, then we lack the information necessary to make an accurate estimate of its true momentum, or even to identify which of the jet constituents belong to the W . This effect is often referred to as an *acceptance* issue due to the finite purview of the final state reconstruction.

To alleviate this issue and provide better control over the inference stage, we propose an alternative target 4-vector that we call the *contained true W momentum* p_{cont}^W , equal to the total 4-momentum of the *truth-level W decay products* that fall within the radius of the final reconstructed top jet. In the truth-level dataset, this is simply $p_{\text{cont}}^W = \sum_k p_{i_k}$ where i_k are the indices of the constituents whose parent is the W -boson and not the b -quark. In the `DELPHES` dataset, however, there is no simple analytic relationship between p_{cont}^W and the jet constituents p_i . That is to say that the mapping of the truth-level information to the detector-level reconstruction is highly non-linear. Nonetheless, in either dataset this vector more accurately reflects the available information about the W -boson and allows us to make inferences not only about the W -boson itself, but also about the containment qualities of the event. This will be discussed further in the Section 5.5 below. For reference, the true mass spectra of both p_{true}^W and p_{cont}^W are shown in Fig. 3. For fully-contained (FC)

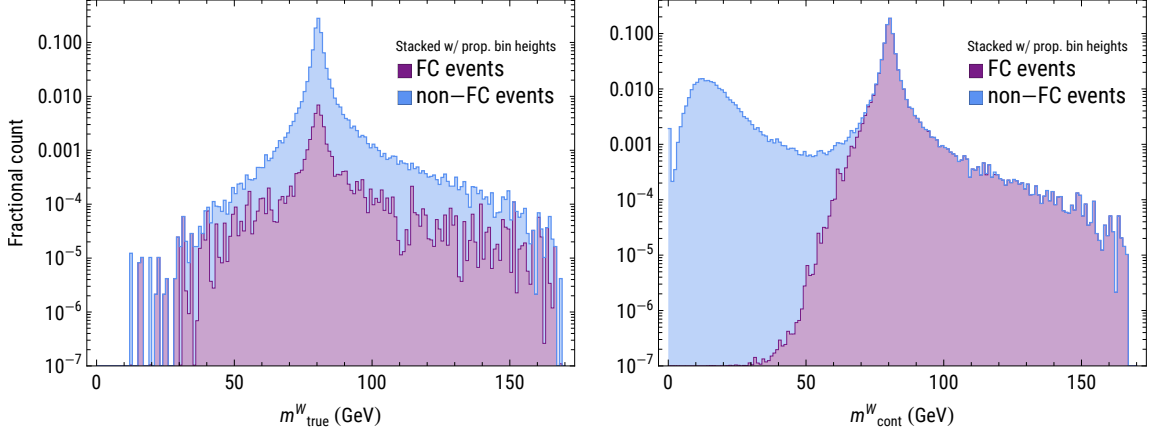


Figure 3: Stacked histogram with proportional bin heights showing the mass spectrum of the two targets, the true W -boson p_{true}^W , and the contained true W momentum p_{cont}^W . The top curve represents the spectrum over the entire dataset on log scale and the bottom curve shows the spectrum over FC events only, *scaled linearly* relative to the top curve, i.e. the fraction of FC events in a given bin is given by the apparent height of the FC curve divided by the total height of the bin (heights are measured from the x -axis). The two mass spectra of FC events, in fact, match.

	Method	σ_{p_T} (%)	σ_m (%)	$\sigma_{\Delta R}$ (centirad)
Without DELPHES	JH	0.66%	1.26%	0.216
	PELICAN JH	0.26%	0.57%	0.113
	PELICAN FC	0.30%	0.71%	0.139
	PELICAN	0.79%	1.12%	0.473
With DELPHES	JH	9.8 %	8.3 %	9.6
	PELICAN JH	3.5 %	2.6 %	2.8
	PELICAN FC	4.0 %	2.9 %	3.1
	PELICAN	5.1 %	3.0 %	4.7

Table 3: Momentum reconstruction results for the Johns Hopkins (JH) tagger and PELICAN trained to reconstruct p_{true}^W . We report the relative p_T and mass resolutions, and the interquartile range for the angle ΔR between predicted and true momenta. PELICAN uncertainties are within the last significant digit.

events, the mass spectra are similar between the true and the contained W mass as expected. Non-FC events are mostly confined to a clear second peak at 13 GeV corresponding to qb and q jets (where one of the quarks from $W \rightarrow qq$ fell outside the jet), and a minor peak at $m_{\text{cont}}^W = 0$ corresponding to b jets.

Given the above observations, we prepared two PELICAN models, one trained to reconstruct p_{true}^W , and another trained to reconstruct p_{cont}^W . Otherwise the two models are identical and are trained in the same way and with the same loss function. We then compare the outputs of each model to p_{true}^W and analyze the benefits of the two choices of the target.

5.3 Regression results for p_{true}^W reconstruction

The results are summarized in Table 3. We quantify the precision of the reconstruction by the transverse momentum¹, p_T , and mass resolutions, given by half of the central 68th interquartile range of $(x_{\text{predict}} - x_{\text{true}})/x_{\text{true}}$, where x is m or p_T . In addition we report the lower 68th interquartile range for ΔR , the z -boost-invariant spatial angle between predicted and true momenta².

¹where $p_T = \sqrt{p_x^2 + p_y^2}$

²where $\Delta R = \sqrt{(\Delta\phi)^2 + (\Delta \ln \tan \theta/2)^2}$

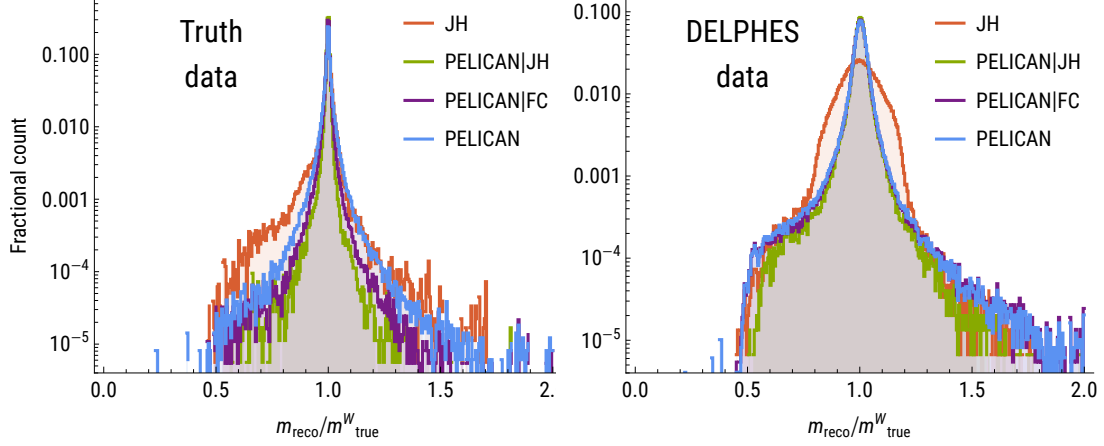


Figure 4: Reconstructed W mass relative to true W mass for the PELICAN model trained on truth (left) or DELPHES (right) data, and targeting p_{true}^W .

Since there are no ML-based methods for this task, we use the W -boson identification of the Johns Hopkins top tagger [43] implemented in FASTJET [42] for the baseline comparison. The tagger has a 36% efficiency on the truth-level dataset and 31% on the DELPHES one. It can only identify W -boson candidates for jets it tags, so we report PELICAN results both on the JH-tagged jets only (PELICAN|JH) and on the full dataset (PELICAN). Moreover, we evaluate PELICAN on the population of FC events (PELICAN|FC). More than 99.9% of JH-tagged events contain all three true quarks $bq\bar{q}$ within the jet radius, so this population represents an especially restricted and ‘ideal’ type of event. The results were evaluated over 5 training runs initialized with different random seeds, and the resolutions reported in Table 3 are consistent across the runs.

There are significant differences in PELICAN’s performance on the different sub-populations of events. In the direct comparison with the JH tagger, PELICAN|JH is 2-4 times more precise. However, even on the much larger class of FC events, PELICAN produces predictions with almost the same precision. The highest loss of precision happens on non-FC events where many of the W decay products are missing from the jet, leading to lower average precision on the entire dataset. As we will discuss in Section 6, this result can be explained by interrogating the PELICAN weights and kinematic information directly.

In Fig. 4 we show the relative reconstructed W masses for two of the models, one trained on truth data, and one on DELPHES data. The results also include the curve for the JH tagger’s reconstruction, as well as PELICAN|JH and PELICAN|FC. The 68th interquantile ranges of these curves match the numbers in the σ_m column of Table 3. See Section 7 for further details on the causes of performance degradation in the DELPHES case. For the complete set of results see Appendix A.

5.4 Regression results for p_{cont}^W reconstruction

Now we train new models with the target vector set to the contained true W momentum p_{cont}^W , evaluate their precision by comparing the outputs to the true W momentum p_{true}^W , and compare the results to Table 3. As shown in Table 4, the resolutions for these models on JH-tagged and FC events are slightly worse than the first set of models, in the DELPHES case by 5-15%. The largest change is in non-FC events, leading to poor average resolutions on the whole dataset. Despite this, as we will now show, these models can in fact be better suited for real-world applications.

5.5 Discussion

To see the main benefit of this model, we present the behavior of the relative reconstructed mass shown in Fig. 5. PELICAN-reconstructed masses within the range of true W masses are almost as precise on the full dataset as they are on FC events (see Fig. 5 near the peak at 1). The most prominent feature obvious from these results is that, despite the slightly lower accuracies on FC events (at fixed width and depth of the network), the

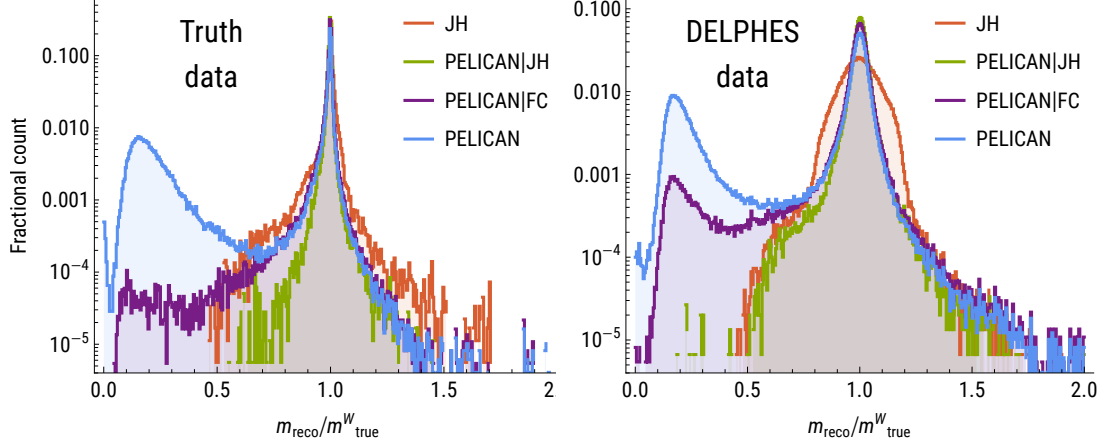


Figure 5: Reconstructed W mass relative to true W mass for the PELICAN model trained (on truth or DELPHES data) targeting p_{true}^W .

	Method	σ_{p_T} (%)	σ_m (%)	$\sigma_{\Delta R}$ (centirad)
Without DELPHES	JH	0.66%	1.26%	0.216
	PELICAN JH	0.27%	0.62%	0.113
	PELICAN FC	0.34%	0.86%	0.142
	PELICAN	2.37%	38.93%	0.681
With DELPHES	JH	9.8 %	8.3 %	9.6
	PELICAN JH	3.6 %	2.8 %	3.1
	PELICAN FC	4.2 %	3.6 %	3.4
	PELICAN	6.2 %	39.6 %	5.6

Table 4: PELICAN resolutions for models trained to reconstruct p_{cont}^W . Resolutions are still obtained by comparing the model predictions to p_{true}^W .

model trained to reconstruct p_{cont}^W accurately reproduces the mass spectrum of m_{cont}^W in Fig. 3 and therefore discriminates between FC and non-FC events, allowing us to perform post-inference event selections.

For instance, in the DELPHES case, choosing a 55 GeV cutoff, 97% of all FC events have $m_{\text{reco}} > 55$ GeV, and vice versa, 97% of all events with $m_{\text{reco}} > 55$ GeV are FC. In this manner we can significantly improve the accuracy of the reconstruction without accessing truth-level information that is needed to identify FC events. This comes at the cost of a modest reduction in signal efficiency – from the ostensible 100% down to 75%. Note that in the DELPHES case, the set of FC events is contaminated with a small number of events with significant losses of W decay products due to detector effects, but it can be refined by reducing the jet radius used in the definition of full containment. Consequently, we propose the following simple routine for real-world applications of these models. First, use the model trained targeting p_{cont}^W as an FC-tagger to refine the data. Then, apply the model targeting p_{true}^W to reconstruct the W -boson.

We conclude that p_{cont}^W is the better target for many common reconstruction tasks where one is willing to sacrifice some signal efficiency – or to only fully measure the 4-momentum on a sub-sample of the identified events – to gain improved accuracy. In the following sections we will not present models trained on both targets, however a complete set of metrics and results, including models targeting p_{true}^W , can be found in Appendix A.

6 W -boson mass measurement

As we saw above, PELICAN is able to reconstruct the mass of the W -boson, m_W , found within the dense environment of the complete decay products of a top quark jet. For truth-level datasets, the resolution of this

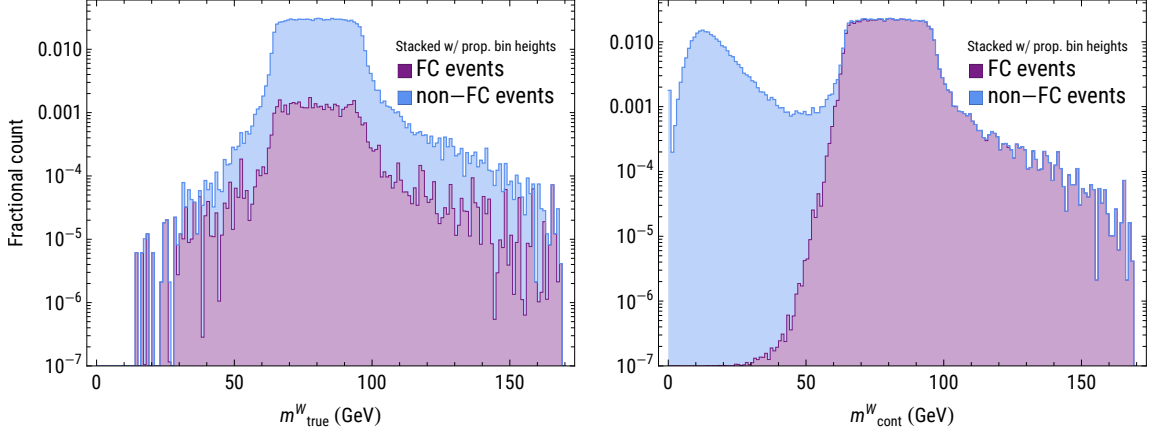


Figure 6: Stacked histogram with proportional bin heights (see description in Fig. 3) showing the mass spectrum of the two targets, p_{true}^W and p_{cont}^W , in the variable W mass dataset.

	Method	σ_{pT} (%)	σ_m (%)	$\sigma_{\Delta R}$ (centrad)
Without DELPHES	JH	7.98%	4.75%	22.180
	PELICAN JH	0.27%	0.63%	0.111
	PELICAN FC	0.35%	0.89%	0.143
	PELICAN	2.64%	39.00%	0.744
With DELPHES	JH	16.0 %	12.0 %	25.4
	PELICAN JH	4.2 %	6.5 %	3.4
	PELICAN FC	4.9 %	8.0 %	3.8
	PELICAN	7.3 %	40.7 %	6.7

Table 5: PELICAN resolutions for models trained to reconstruct p_{cont}^W with variable m_W . Resolutions are still obtained by comparing the model predictions to p_{true}^W .

reconstruction is below the natural width of the mass spectrum. In the **DELPHES** case, the resolution is too wide to produce any substantial correlation between the true and reconstructed masses (see Appendix A for figures that demonstrate this). We would like to eliminate the possibility that the reason that the true masses are highly concentrated around 80 GeV is due in part to the potential for PELICAN to effectively *memorize* a single number: the W -boson mass. In this section we examine a more realistic reconstruction task, where the true mass of the target particle is unknown, and the dataset uniformly covers a wide range of its masses.

The reconstruction task is still identical to that of Section 5. Even though we could use a scalar-valued version of PELICAN to target the mass of the W -boson, the accuracy of that reconstruction would in fact suffer in comparison with the 4-vector model. This is simply due to the fact that the 4-momentum contains more relevant information than the mass alone, since the direction and the energy of the particle are, in part, correlated with the mass. Thus the only new element in this experiment will be the dataset, which will now involve W -bosons of varying masses uniformly covering the range $m_W \in \{65, 95\}$ GeV. The dataset is also identical to that used in Section 5, except that the W -boson mass is set to be variable. This is achieved by combining multiple independently-produced datasets where the generator-level value of m_W was modified from its default value. Fig. 6 shows the resulting distribution of W -boson masses, as well as that of the sum of W daughters contained within each jet.

6.1 Regression results for m_W reconstruction

The hyperparameters and the training regime used here are the same as in Section 5. Here we focus on the model trained to reconstruct the contained momentum p_{cont}^W (see Appendix A to find the results for the model targeting p_{true}^W). The outputs are then compared to the true W -boson p_{true}^W . The accuracies for the full 4-vector reconstruction are presented in Table 5. The largest loss of accuracy relative to Section 5 is, unsurprisingly, in

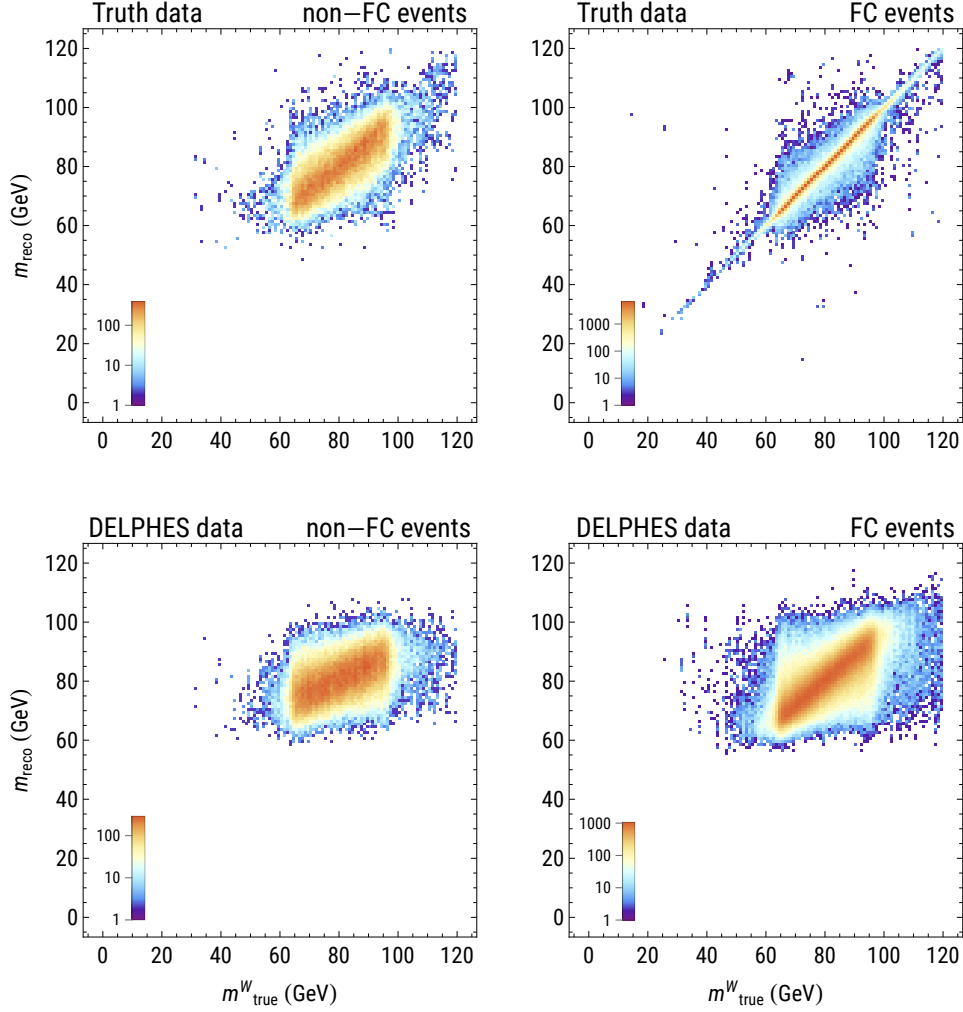


Figure 7: 2D histograms of true vs. reconstructed masses for models trained on the variable mass dataset targeting p_{true}^W (top: truth data; bottom: **DELPHES** data), broken up into two populations based on jet containment (left: non-FC events; right: FC events).

the mass column. However, since the true mass now covers a much wider range, this still presents a significant improvement in the mass reconstruction capability. To demonstrate this better, we show the 2D correlations between target and reconstructed masses in Figures 7 and 8 for the models trained targeting p_{true}^W and p_{cont}^W , respectively. We also differentiate between non-FC (left) and FC (right) events in the two sides of each of the panels in each figure.

6.2 Model complexity

The model examined above has 210k trainable parameters, however even significantly smaller models achieve good accuracy. As an illustration, we compare the resolutions of three **PELICAN** models trained on the variable mass dataset targeting p_{true}^W . They are obtained from the original model by a proportional rescaling of the widths of all layers. The first model is the 210k parameter one, with 132/78 channels, i.e. each messaging layer has 132 input and 78 output channels. The second model has 60/35 channels and 49k parameters. The third model has 25/15 channels and 11k parameters. The resolutions over the **DELPHES** test dataset are reported in Table 6, and we observe that even the 11k-parameter model handily beats the JH method.

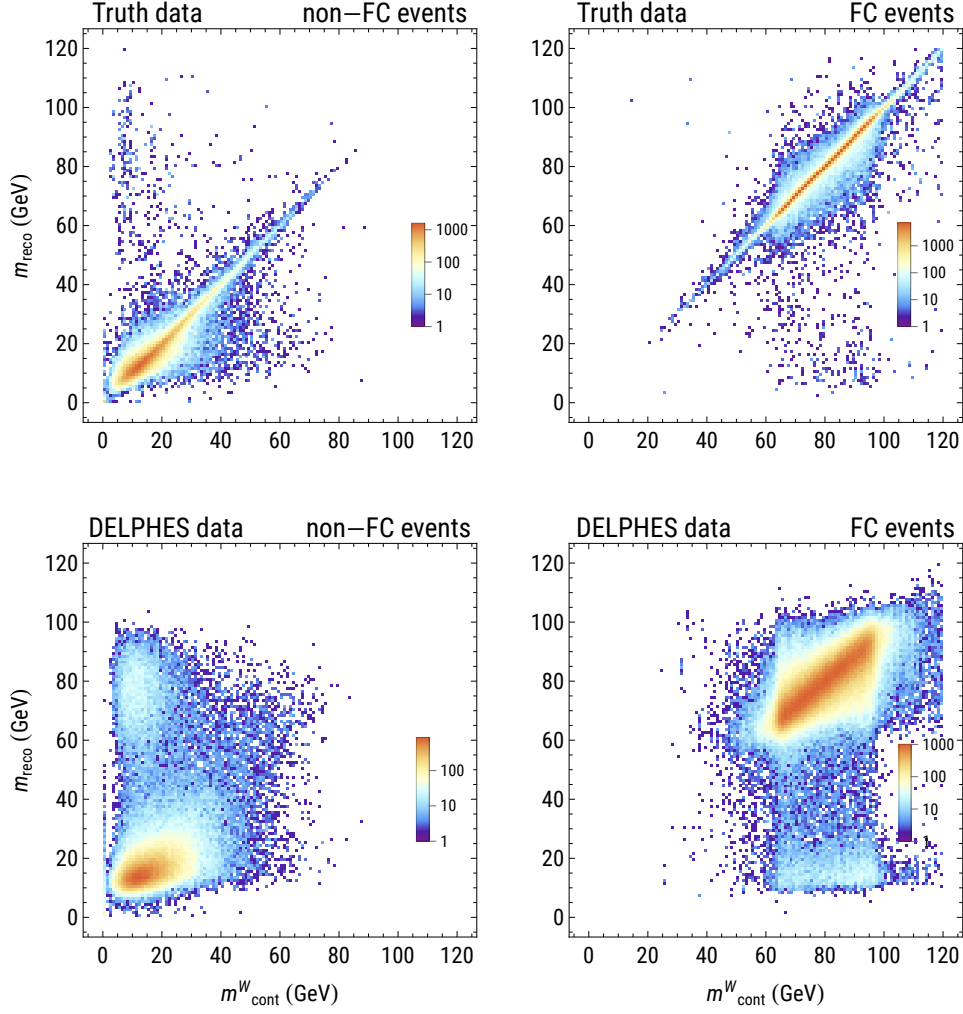


Figure 8: 2D histograms of target vs. reconstructed masses for models trained targeting p_{cont}^W (top: truth data; bottom: DELPHES data), broken up into two populations based on jet containment (left: non-FC events; right: FC events).

# params	σ_{p_T} (%)	σ_m (%)	$\sigma_{\Delta R}$ (centirad)
210k	6.1 %	8.2 %	2.8
49k	6.5 %	8.6 %	3.2
11k	7.4 %	9.5 %	3.8

Table 6: Comparison of PELICAN models of three different network widths trained to reconstruct p_{true}^W with variable W mass. Tested on DELPHES data.

6.3 Discussion

In the DELPHES dataset, we observe that for non-FC events (bottom left of Fig. 8), the reconstructed contained mass is only weakly correlated with the true contained mass (or with the true W mass, as shown in Fig. 22 in Appendix A). However, in the quadrant where both masses exceed 55 GeV, we find a 65% correlation on FC events in the DELPHES case. The most important type of error PELICAN makes here is when a non-FC event gets assigned a high reconstructed mass. Meaning that a mass near that of the true W was assigned for a jet with few of the W decay products in it. Among all events with $m_{\text{reco}} > 55$ GeV, 3.6% are non-FC, and

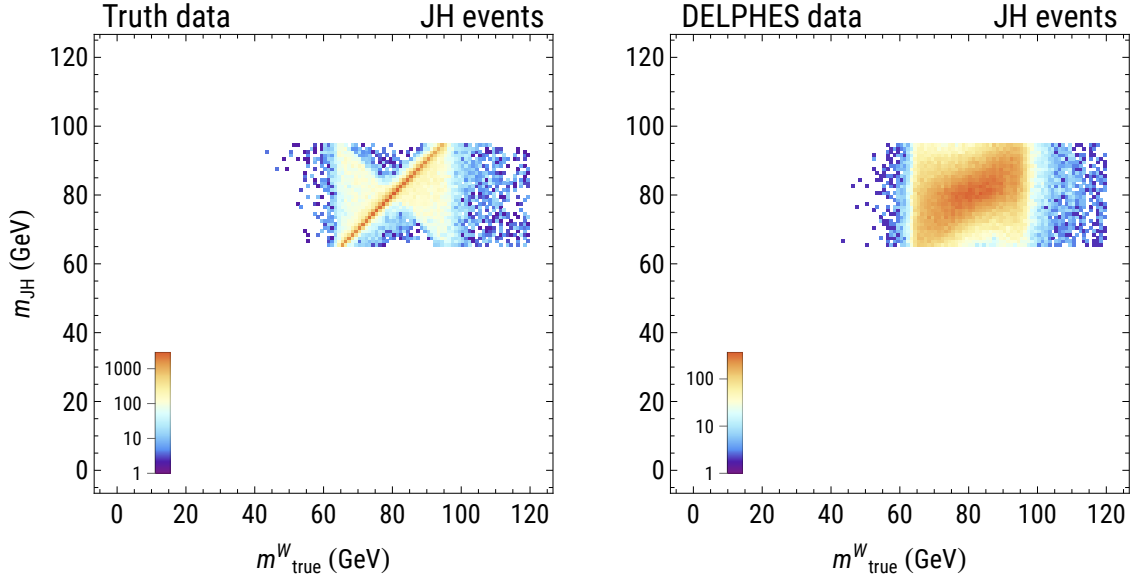


Figure 9: JH tagger’s reconstruction of the W mass on the variable W mass dataset, truth-level and **DELPHES** versions. The correlation values are 47% and 25%, correspondingly.

they bring the correlation among that population down to 51% (p_T , mass, and angular resolutions on this population closely track those of **PELICAN**|FC above). But since in practice we’re interested in m_{true}^W , the correlation between that and m_{reco} is higher, at 59% among events with $m_{\text{reco}} > 55$ GeV. This is a significant improvement over the model trained on the original $m_{\text{true}}^W \sim 80$ GeV **DELPHES** dataset, and especially over non-ML methods such as the JH tagger (see Fig. 9). However, even a model trained on **DELPHES** data to reconstruct p_{true}^W , in fact, achieves a 40% correlation with m_{true}^W on non-FC events (see Fig. 7), so FC-tagging may not be necessary. Overall, **PELICAN** provides a viable method for estimating particle masses.

7 **PELICAN** explainability

Despite the output of the **PELICAN** regression model ostensibly being a 4-vector (or multiple 4-vectors), the richer and more natural object to treat as the output are the **PELICAN** weights $\{c_i\}$ introduced in (Eq. 5.1). Each c_i is attached to its corresponding input constituent p_i due to permutation equivariance and therefore encodes *a scalar feature of that particle within the event*. As we will show in this section, the behavior of these weights is key to the unique explainability and visualization features of the **PELICAN** architecture.

In essence, **PELICAN** is able to take a set of N input 4-vectors and assign N scalar features to them (of course there can be several features per input as well) in a Lorentz-invariant way. This can be powerful in a variety of applications, but in the context of particle reconstruction the problem of finding the right values of the weights is similar to a soft clustering problem. Assuming an idealized dataset with perfect information about the decay products, the model should identify the decay products of the W -boson, assign $c_i = 1$ to them, and zero to all other constituents. This is analogous to what taggers like the Johns Hopkins top-tagger aim to do via jet clustering. However, since any five 4-vectors are linearly dependent, there is a continuum family of solutions $\{c_i\}$ and it is not clear that **PELICAN** will prefer the clustering solution.

7.1 Distributions of **PELICAN** weights

In Fig. 10 we display the distributions of all **PELICAN** weights for models from Section 5 trained targeting p_{true}^W . We also mark each constituent as either a W - or a b -daughter. This yields several observations.

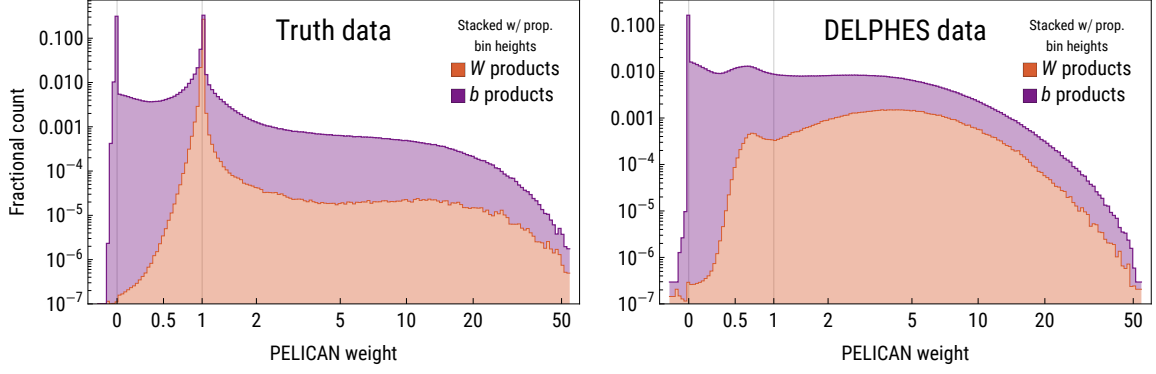


Figure 10: Stacked histograms with proportional bin heights of all PELICAN weights computed over the testing dataset for the 4-vector reconstruction task from Section 5 using models trained targeting p_{true}^W . Broken up into two populations – W -boson products and b -quark products. In the DELPHES case, a constituent is considered a W product if the corresponding calorimeter cell detected at least one true W daughter.

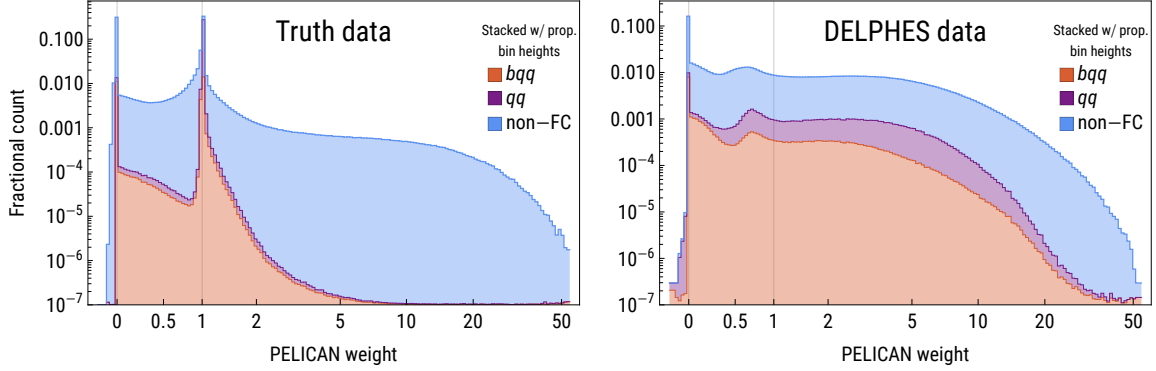


Figure 11: Stacked histograms with proportional bin heights of all PELICAN weights computed over the testing dataset for the 4-vector reconstruction task from Section 5 using models trained targeting p_{true}^W . Broken up into three populations by jet containment: bqq events (all three truth-level quarks from the $t \rightarrow bW \rightarrow bqq$ process fall within the jet clustering radius); qq events (only the b -quark fell outside of the jet); and non-FC events, which include bq , b , and q events.

Firstly, nearly all weights are either non-negative or very slightly negative (e.g. above -0.1) with a very sharp peak at zero (the peak is entirely to the left of zero to very high precision³). This is the first feature that justifies the interpretation of PELICAN as a *soft clustering* method. Since our inputs represent realistic events, all input 4-vectors in them are causally related, and in particular they belong to the future light cone, as does the target vector. This implies that no linear combination of these vectors with positive coefficients can produce a zero vector. The distributions, therefore, show that PELICAN weights assigned to b -daughters are not “contaminated” with these degenerate combinations.

Secondly, the truth-level distribution is highly concentrated at 0 and 1 and very closely matches the binary clustering solution. That is, almost all constituents assigned weight 0 are b -daughters, and almost all of those assigned 1 are W -daughters. Nevertheless, 30% of b -daughters are assigned positive weights, prompting further investigation. Moreover, the distribution of W -daughter weights in the DELPHES case is so spread out that it becomes difficult to explain it by a mere analogy with clustering.

We can delve more deeply into the weight distribution by evaluating the sub-populations of weights based on jet containment. Fig. 11 shows the distributions of weights for bqq , qq , and non-FC events. The majority of constituents at the high end of the weight scale belong to non-FC events. Similarly, the weights

³The bin $[-10^{-6}, 0)$ contains about 100 times more constituents than the bin $[0, 10^{-6})$.

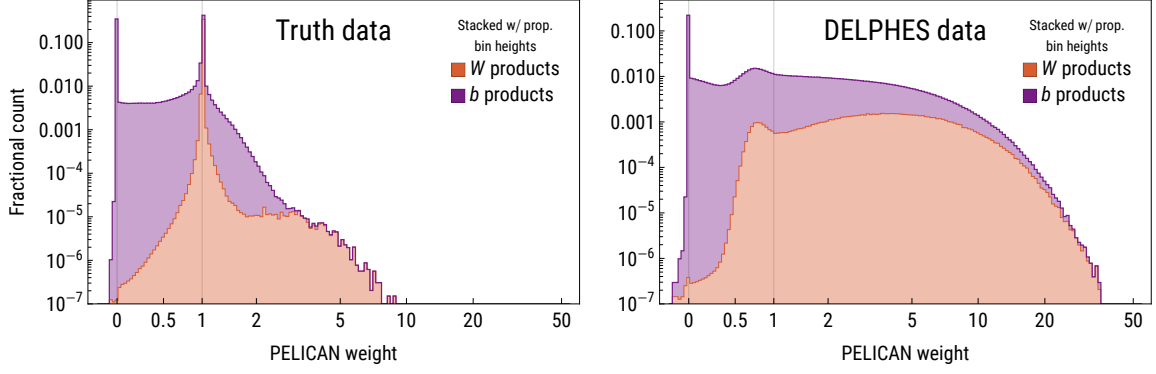


Figure 12: Stacked histograms with proportional bin heights of all PELICAN weights for the 4-vector reconstruction task from Section 5 using models trained targeting p_{cont}^W . Broken up into two populations by parent type.

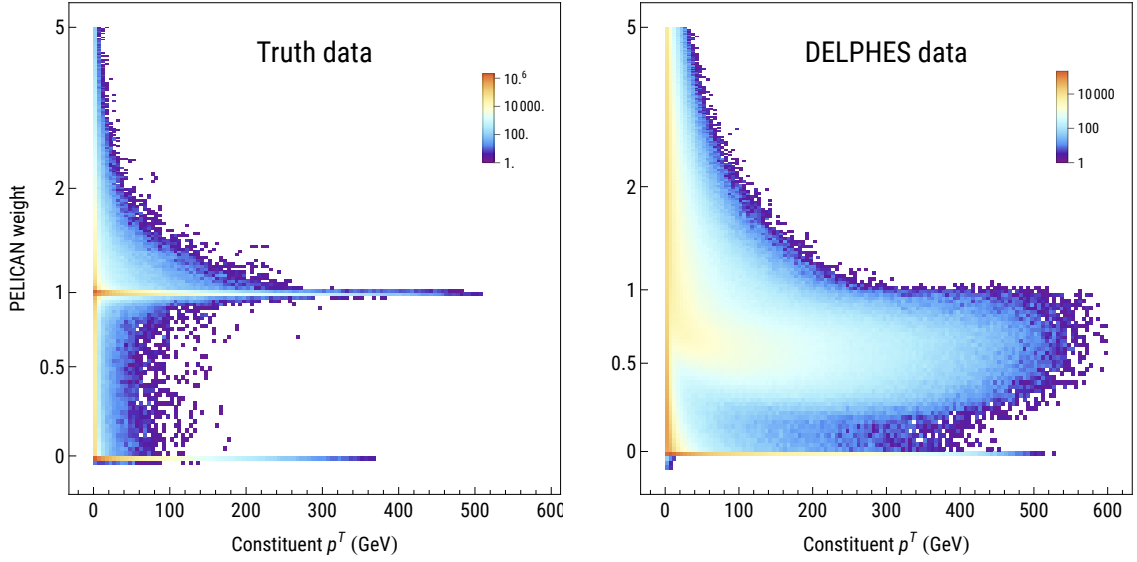


Figure 13: 2D histogram of PELICAN weights vs constituent transverse momentum for the 4-vector reconstruction task from Section 5 using models trained targeting p_{cont}^W . Only FC events shown here.

produced by the models trained targeting p_{cont}^W , shown in Fig. 12, are more highly concentrated at 0 and 1, and have much lower and shorter “tails” on the right, especially among b -daughters. This is the first indication that PELICAN tends to up-weight some constituents in events where it doesn’t have enough information for an accurate reconstruction.

This approach allows to characterize the constituents that are being up-weighted. Fig. 13 shows the constituent weights as a function of the constituent’s p_T . The main observation here is that among high-energy (“hard”) constituents with $p_T > 100$ GeV the weight distribution is much more binary, and the vast majority of constituents with weights falling away from the two peaks are soft, below 20 GeV. In the DELPHES case PELICAN appears to down-weight high-energy W -daughters and up-weight soft constituents. Once again, loss of information in the form of detector effects appears to lead to PELICAN up-weighting soft constituents.

7.2 Detector effects on PELICAN weights

While the truth-level PELICAN models reliably converge to a binary clustering solution, the weights in the DELPHES case do not permit such a straightforward interpretation. To better understand their behavior, we

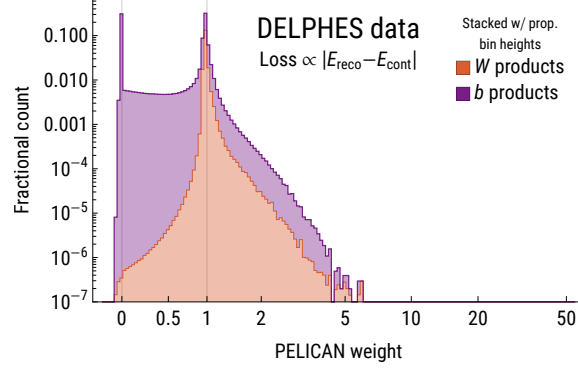


Figure 14: Same as Fig. 12 but this time the model is trained using a single-term loss function proportional to $|E_{\text{reco}} - E_{\text{cont}}|$.

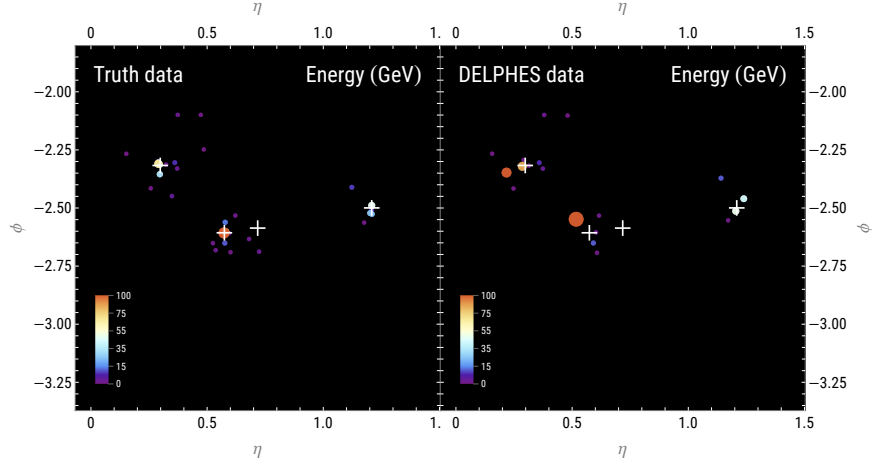


Figure 15: A single event viewed in the η, ϕ plane with color and size dependent on energy. The central cross marks the true W boson, and the other three crosses mark the three true quarks from the process $t \rightarrow bqq$.

ran additional experiments using custom datasets that exclude different components of the **DELPHES** detector simulation one by one. **DELPHES** performs the following steps: simulate the effect of the magnetic field B_z on charged final-state particles; aggregate truth-level particle energies within each electromagnetic calorimeter (ECAL) and hadronic calorimeter (HCAL) detector cell; apply energy smearing by sampling a lognormal distribution; unify the ECAL and HCAL cells; apply spatial smearing by picking a uniformly random point within the detector cell; construct the spatial momentum so that the resulting 4-vector, which represents a detector cell, is massless. We found that while each of these steps contributes to smearing out the truth-level distribution of PELICAN weights and shifting the peak downwards, the magnetic field is responsible for almost all of the differences between truth and **DELPHES** results.

The simulated magnetic field is able to deflect charged particles very significantly, enough to account for most of the error in PELICAN’s reconstruction relative to the truth-level reconstruction. Our hypothesis for why this leads to lower PELICAN weights for hard constituents is the following. Deflected hard particles produce large errors in the direction but not the energy of the reconstruction, therefore one can down-weight them and compensate for the energy deficit using softer constituents. Moreover, by up-weighting softer constituents PELICAN can in fact partially correct the error in the direction since the deflections of positively charged particles can be partially cancelled out by those of negatively charged particles.

An extra piece of evidence in support of this hypothesis can be found by modifying the loss function. If we re-train the model on the same **DELPHES** dataset using a loss function consisting of a single energy term $|E_{\text{reco}} - E_{\text{true}}|$, we find a distribution of weights (see Fig. 14) nearly as bimodal as the original one trained on

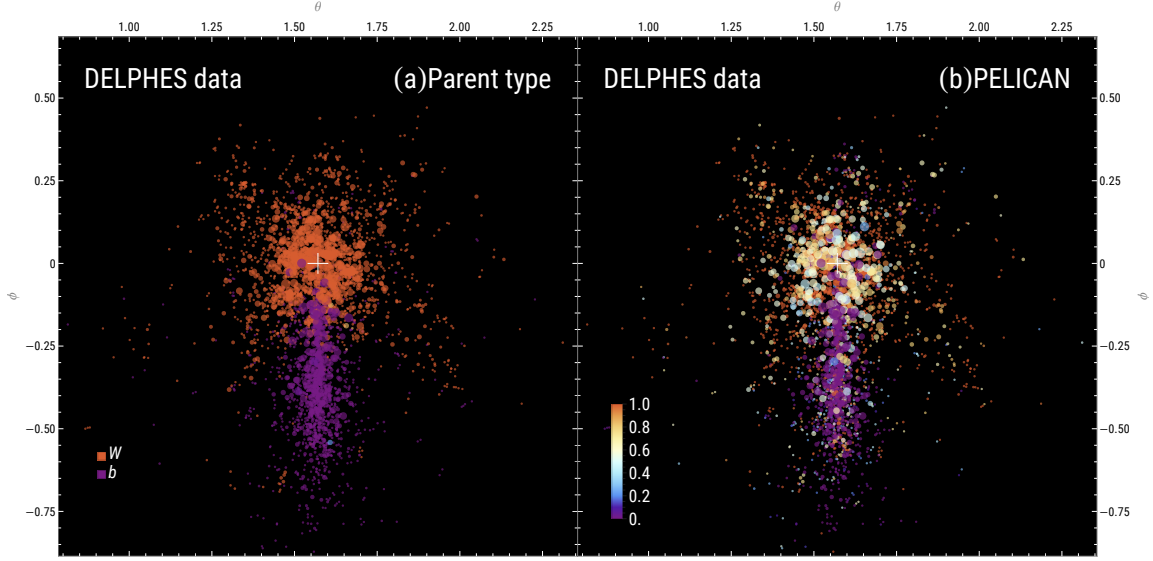


Figure 16: Composite event display of 200 events from the `DELPHES` dataset from Section 5. Each event is transformed using a 3D rotation matrix such that the true W boson ends up at $(\theta, \phi) = (\pi/2, 0)$ (white cross), and the true b -quark is directly below. `PELICAN` is rotationally invariant, so its output is unaffected by the normalization. Each dot is a `DELPHES` constituent and the dot size increases logarithmically with constituent energy. (a) Color reflects parent type: constituents that are fully derived from W -daughters are orange and those from b -daughters are purple; in the rare cases when the fraction of W -derived energy in a given calorimeter cell is between 0 and 1, the corresponding color is taken from the color scale in the right pane. (b) Color reflects the value of the `PELICAN` weight, clipped to the interval $[0, 1]$, as shown in the legend. Note how the hardest W constituents (largest dots) tend to have `PELICAN` weights between 0.5 and 1.

truth-level data (see Fig. 12). This indicates that the source of the error in `PELICAN`’s reconstruction on `DELPHES` data is overwhelmingly *spatial*. Out of all the steps that `DELPHES` performs, only two are purely spatial: momentum smearing within one cell, and the simulated magnetic field. However, the detector cells (approximately 0.02×0.02 in (η, ϕ)) are much smaller than the magnitude of `PELICAN`’s typical angular error, and thus smearing cannot explain the error.

7.3 Event visualization

As we discussed above, despite being a single-vector regression model, `PELICAN` produces one feature *per input constituent* (namely the weight c_i), and these features become interpretable by virtue of Eq. 5.1. This gives us a unique opportunity to make event-level visualizations that provide insight into how `PELICAN` treats jet topology and how it compares to conventional methods such as the JH tagger’s jet clustering.

In Fig. 16 we show an amalgamation of 200 events from the `DELPHES` dataset from Section 5 projected onto the unit sphere. Each event was spatially rotated so that the position of the true W within the image is fixed and the true b -quark is located in the negative ϕ direction. In one display the constituents are colored according to their parent being either the W boson or the b -quark, and in the other they’re colored based on their assigned `PELICAN` weight. The correlation between the two images is clear: b -daughters tend to be correctly assigned zero weight, whereas W -daughters have positive weights with the hardest constituents having weights between 0.4 and 0.8.

In Fig. 15 we show a single event in the (η, ϕ) plane, with dot color and size dependent on the constituent energy. Note the reduced number of constituents in the `DELPHES` display, and how some of the constituents get strongly deflected by the simulated magnetic field. The same event can be visualized in three more helpful ways. In addition to parent type and `PELICAN` visualizations introduced in Fig. 16, we can also extract the list of constituents that the JH tagger identifies as belonging to the W boson and highlight them. Fig. 17 displays the same single event in all three ways. In addition, we add a special marker for the direction of the

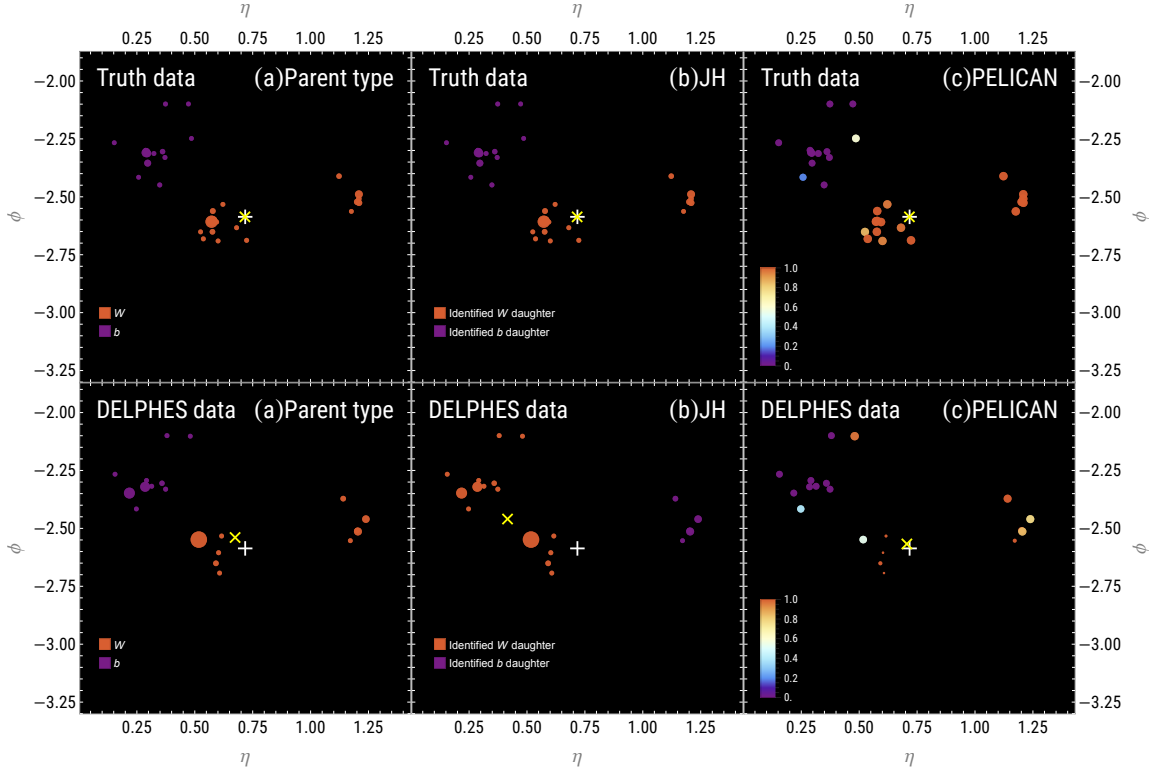


Figure 17: The same event as in Fig. 15 in the (η, ϕ) plane. (a) Constituents are colored according to the actual parent type; size increases with energy; the yellow cross marks the reconstruction obtained by summing all of the constituents that belong to the W boson. (b) Constituents are colored according to how they are tagged by the JH-tagger as either W -daughters or not; size increases with energy; the yellow cross marks the JH-reconstructed W boson. (c) Constituents are colored according to their PELICAN weight clipped to the interval $[0, 1]$; size increases as the weight goes from 0 to 1 and decreases after that. Note how the soft DELPHES W -constituents get assigned high PELICAN weights.

reconstructed W boson. In the parent type pane, this reconstruction is defined as $\sum_{i=1}^N r_i p_i$ where r_i is the energy of the true W -daughters within that constituent divided by the actual energy of the constituent. In the JH and PELICAN panes, the marker corresponds to the corresponding reconstructions obtained by those methods.

8 IRC-safety and PELICAN

Perturbative computations in QCD suffer from a divergence caused by two types of processes: soft emission and collinear splittings. As a consequence, meaningful observables in this theory need to be insensitive to such processes, and this requirement is known as IRC-safety. In this section we provide a precise definition, give a characterization of IRC-safe Lorentz-invariant observables (see details in Appendix B), and describe modifications to the PELICAN architecture that make it IR-safe or IRC-safe.

Infrared safety (IR-safety) guarantees insensitivity to soft emissions, i.e. particles with relatively low energies and momenta. A family of continuous symmetric observables $f^{(N)}(p_1, \dots, p_N)$ is said to define an IR-safe observable f if

$$\lim_{\epsilon \rightarrow 0} f^{(N+1)}(p_1, \dots, p_N, \epsilon p) = f^{(N)}(p_1, \dots, p_N) \quad (8.1)$$

for any N and any p_1, \dots, p_N, p , where ϵ controls how infinitesimally small the considered soft emission p is.

Collinear safety (C-safety) is a restriction on observables in perturbative QCD that arises from the divergent contributions of collinear emissions of gluons. Positive gluon mass would prevent such divergences, which is why C-safety concerns only massless particles. We can define C-safety formally as follows: an observable $f(p_1, \dots, p_N)$ is C-safe if, whenever two massless 4-momenta p_1 and p_2 become collinear (which happens for massless particles iff $p_1 \cdot p_2 = 0$), the value of f depends only on the total momentum $p_1 + p_2$. Expressed even more explicitly, C-safety says that setting $p_1 = \lambda p$ and $p_2 = (1 - \lambda)p$ with some 4-vector p such that $p^2 = 0$ must lead to the same output regardless of the value of λ , i.e.

$$C_{12}(p)f = \partial_\lambda f(\lambda p, (1 - \lambda)p, p_3, \dots, p_N) = 0. \quad (8.2)$$

In Appendix B we characterize IRC-safe Lorentz-invariant observables, but the following summary will suffice for the purpose of designing an IRC-safe version of PELICAN. First, a Lorentz-invariant observable (assumed to be consistently defined for any finite number N of 4-vector inputs) is IR-safe if and only if it has no explicit dependence on the multiplicity N . More precisely, adding the zero 4-vector to the list of inputs should leave the output value invariant. Second, an IRC-safe Lorentz-invariant observable is one that is IR-safe and moreover depends on any of its massless inputs only through their total. E.g. if p_1, p_2, p_3 are fixed to be massless, then $f(p_1, p_2, p_3, p_4, \dots)$ must depend only on $p_1 + p_2 + p_3$. In particular, if all inputs are massless, then all IRC-safe invariant observables are functions of only the jet mass $M^2 = (\sum_i p_i)^2$. Note, however, that such an observable can still depend on these vectors in an arbitrarily complex fashion away from the massless manifold.

The original PELICAN architecture as introduced above is neither IR- nor C-safe. Below we modify the architecture to make it exactly IR-safe or IRC-safe and evaluate the implications.

8.1 IR-safe PELICAN

As shown above, IR-safety in Lorentz-invariant networks essentially requires the outputs to be independent of the multiplicity N . There are four ways in which the multiplicity shows up in PELICAN:

1. Scaling with $N^\alpha / \bar{N}^\alpha$ in the equivariant block. This must be disabled for IR-safety.
2. Non-zero bias values in linear layers. Since the network is permutation-equivariant, the bias values are shared across jet constituents, which means that upon aggregation in the following equivariant layer they contribute multiples of N . All biases in all linear layers must be disabled for IR-safety.
3. The input embedding must map zero to zero, but our original choice already satisfies this. In addition, the activation function must also have a fixed point at zero. Our default choice, LeakyReLU, also satisfies this.
4. Following an application of a PELICAN equivariant block, rows and columns corresponding to soft constituents will contain a combination of sums over all constituents. Even in the absence of biasing constants, this effectively increases the multiplicity with which these values enter in the later aggregations. This can be resolved by making sure that rows and columns that are soft at the input remain soft throughout the whole network. Therefore we introduce *soft masking*, whereby the last 12 equivariant aggregators (those don't preserve the softness of rows/columns) are followed by a multiplication by the vector of values $J \cdot p_i$, where $J = \sum_{i=1}^N p_i$, scaled and clipped to be within $[-1, 1]$. In Eq_{2→2} this multiplication is applied both row-wise and column-wise, and in Eq_{2→1} it's component-wise.

With these modifications, PELICAN becomes IR-safe. As we will see, this restriction leads to a modest reduction in the performance of PELICAN's predictions in our tasks of interest.

8.2 IRC-safe PELICAN

Adding C-safety to the architecture is much simpler. As stated above, the necessary requirement is that the output depend on massless inputs only through their sum. In PELICAN this can be achieved by inserting a linear permutation-equivariant layer with a mass-based soft mask immediately at the input (any nonlinear embedding has to be done later). Consider a case where p_1, p_2 are massless and the dot product matrix $\{d_{ij}\}$ is fed into such an equivariant layer. Most of the aggregators will compute sums over rows or columns, thus immediately producing C-safe quantities. However, several of the aggregators, including the identity, will

preserve individual information about each p_i , therefore their output rows and columns corresponding to p_1 and p_2 need to be thrown out. This can be done by a soft mask that turns to zero as the mass of any input goes to zero. This mask is defined in the same way as the IR mask except using m_i^2 instead of $J \cdot p_i$. It needs to be applied only to the first 2 order zero and the first 7 order one aggregators.

Coincidentally, this soft mask can also be used in place of an IR mask, which means that we only need the C-safe soft mask to make a fully IRC-safe PELICAN architecture. Altogether it gets applied to all equivariant aggregators except the third one (which extracts the diagonal and is thus IRC-safe by definition).

8.3 Testing IR/C-safe PELICAN models

First we quantify the deviation in PELICAN’s outputs that occurs under soft and collinear splittings and observe how training affects them. We define an IR-splitting as adding a zero 4-vector to the list of input constituents. Then PELICAN’s output on IR-split data is directly compared to the original output. Defining a C-splitting is more difficult since realistic events never contain any exactly collinear constituents, and we want to avoid changing the number of particles so as to make this test independent of IR-safety. Therefore we prepare the data by inserting two copies of the vector $(1, 0, 0, 1)$ to each event. Then the C-splitting will amount to replacing these two vectors with $(2, 0, 0, 2)$ and $(0, 0, 0, 0)$. The outputs on the same event prepared in these two ways can be directly compared.

To compare two outputs $p_{\text{reco}}, p'_{\text{reco}}$ we compute the relative deviation $|(p'_{\text{reco}} - p_{\text{reco}})/p_{\text{reco}}|$, where the division is component-wise. To estimate the effect of an IR- or C-splitting on PELICAN’s predictions, we take the median value of this deviation over a batch of events. The same can also be done with PELICAN weights as the outputs. The splittings are applied to 100-event batches of events from one of our datasets and the median deviations are averaged over 300 batches. We test 5 randomly-initialized models and 5 models trained on the full variable W mass dataset from Section 6.

We find that a randomly-initialized PELICAN regression model’s output 4-vector deviates by 0.5%-7% under an IR-split, and the PELICAN weights deviate by up to 5%. However, regression models trained to reconstruct p_{cont}^W have both deviations under 5%, potentially indicating a slight improvement in IR-safety due to training. The resolutions σ_{p_T}, σ_m , and $\sigma_{\Delta R}$ of the trained IR-safe truth-level models are about 20%-35% worse (larger) than the original models, and similarly the DELPHES resolutions get 40%-50% worse. We also note that IR-safe PELICAN models appear to be slightly more rigid under C-splits, showing 5%-16% deviations that enhance slightly to at most 11% after training.

Under a C-splitting, the randomly-initialized regression model’s outputs (both the 4-vector and the weights) consistently deviate by 3%-8%, and the same range of deviations was observed on fully trained models as well. The resolutions of trained IRC-safe truth-level models suffer significantly in comparison to the regular models, exhibiting 5-6 times higher values of σ_{p_T}, σ_m , and $\sigma_{\Delta R}$. We do not perform this comparison for DELPHES models since the jet constituents coming out of DELPHES are massless, so only functions of the jet mass are expressible by IRC-safe PELICAN on that data.

9 Conclusion

We have presented a full description of PELICAN: a network that respects particle permutation and Lorentz symmetries important in particle physics. PELICAN is a general network which is performant at 4-vector regression and provides state-of-the-art performance in the task of top-tagging. To demonstrate PELICAN’s regression capabilities, we chose the reconstruction of the W -boson’s 4-momentum from a full top quark jet, and to our knowledge PELICAN is the first ML method applied to this problem. Even within these tasks there is room to improve PELICAN’s performance by introducing additional scalar information such as particle charges, which would allow the network to account for the simulated collider’s magnetic field. PELICAN’s architecture, its flexibility, and generalizability may also allow for future applications to charged-particle track reconstruction, pile-up identification, and full-event reconstruction. Being a general architecture, PELICAN is not limited to top quark decays or even jets. This network inherently provides powerful tools for investigating its own behavior due to the equivariant architecture and shows promise as a tool which can be thoroughly investigated if deployed in real world scenarios.

10 Acknowledgements

The authors would like to thank the Data Science Institute at the University of Chicago for its generous support of this research. TH is supported by the Department of Physics at the University of Chicago. DWM and JTO are supported by the National Science Foundation under Grant PHY-2013010. The computations in this work were, in part, run at facilities supported by the Scientific Computing Core at the Flatiron Institute, a division of the Simons Foundation. The Center for Computational Mathematics at the Flatiron Institute is supported by the Simons Foundation.

References

- [1] J. Gallicchio and M.D. Schwartz, *Quark and gluon jet substructure*, *JHEP* **2013** (2013) 90.
- [2] A.J. Larkoski, J. Thaler and W.J. Waalewijn, *Gaining (Mutual) Information about Quark/Gluon Discrimination*, *JHEP* **11** (2014) 129 [[1408.3122](#)].
- [3] P.T. Komiske, E.M. Metodiev and M.D. Schwartz, *Deep learning in color: towards automated quark/gluon jet discrimination*, *JHEP* **01** (2017) 110 [[1612.01551](#)].
- [4] E. Alvarez, M. Spannowsky and M. Szewc, *Unsupervised quark/gluon jet tagging with poissonian mixture models*, *Front. Artif. Intell* **5** (2022) .
- [5] G. Kasieczka, N. Kiefer, T. Plehn and J.M. Thompson, *Quark-gluon tagging: Machine learning vs detector*, *SciPost Phys.* **6** (2019) 069.
- [6] J.M. Butterworth, A.R. Davison, M. Rubin and G.P. Salam, *Jet substructure as a new Higgs search channel at the LHC*, *Phys. Rev. Lett.* **100** (2008) 242001 [[0802.2470](#)].
- [7] D.E. Kaplan, K. Rehermann, M.D. Schwartz and B. Tweedie, *Top Tagging: A Method for Identifying Boosted Hadronically Decaying Top Quarks*, *Phys. Rev. Lett.* **101** (2008) 142001 [[0806.0848](#)].
- [8] A. Butter et al., *The machine learning landscape of top taggers*, *SciPost Phys.* **7** (2019) 014 [[1902.09914](#)].
- [9] J. Thaler and L.-T. Wang, *Strategies to identify boosted tops*, *JHEP* **07** (2008) 092 [[0806.0023](#)].
- [10] D.E. Soper and M. Spannowsky, *Finding top quarks with shower deconstruction*, *Phys. Rev. D* **87** (2013) 054012 [[1211.3140](#)].
- [11] I. Feige, M.D. Schwartz, I.W. Stewart and J. Thaler, *Precision Jet Substructure from Boosted Event Shapes*, *Phys. Rev. Lett.* **109** (2012) 092001 [[1204.3898](#)].
- [12] Y.-T. Chien and I. Vitev, *Jet Shape Resummation Using Soft-Collinear Effective Theory*, *JHEP* **12** (2014) 061 [[1405.4293](#)].
- [13] S. Marzani, L. Schunk and G. Soyez, *The jet mass distribution after Soft Drop*, *Eur. Phys. J. C* **78** (2018) 96 [[1712.05105](#)].
- [14] F.A. Dreyer, G.P. Salam and G. Soyez, *The Lund Jet Plane*, *JHEP* **12** (2018) 064 [[1807.04758](#)].
- [15] R. Kogler, *Advances in Jet Substructure at the LHC: Algorithms, Measurements and Searches for New Physical Phenomena*, no. 1615-0430, Springer Cham, 1 ed. (May, 2021).
- [16] J. Thaler and K. Van Tilburg, *Identifying boosted objects with n -subjettiness*, *JHEP* **03** (2011) 015 [[1011.2268](#)].
- [17] CMS collaboration, *First Measurement of Hadronic Event Shapes in pp Collisions at $\sqrt{s} = 7$ TeV*, *Phys. Lett. B* **699** (2011) 48 [[1102.0068](#)].
- [18] P.T. Komiske, E.M. Metodiev and J. Thaler, *Energy flow polynomials: A complete linear basis for jet substructure*, *JHEP* **04** (2018) 013 [[1712.07124](#)].
- [19] R. Kogler et al., *Jet Substructure at the Large Hadron Collider: Experimental Review*, *Rev. Mod. Phys.* **91** (2019) 045003 [[1803.06991](#)].
- [20] S. Marzani, G. Soyez and M. Spannowsky, *Looking inside jets: an introduction to jet substructure and boosted-object phenomenology*, vol. 958, Springer (2019), [10.1007/978-3-030-15709-8](#), [[1901.10342](#)].
- [21] HEP ML Community, “A Living Review of Machine Learning for Particle Physics.”

- [22] A. Butter, G. Kasieczka, T. Plehn and M. Russell, *Deep-learned Top Tagging with a Lorentz Layer*, *SciPost Phys.* **5** (2018) 028 [[1707.08966](#)].
- [23] M. Erdmann, E. Geiser, Y. Rath and M. Rieger, *Lorentz Boost Networks: Autonomous Physics-Inspired Feature Engineering*, *JINST* **14** (2019) P06006 [[1812.09722](#)].
- [24] P.T. Komiske, E.M. Metodiev and J. Thaler, *Energy flow networks: deep sets for particle jets*, *JHEP* **2019** (2019) 121 [[1810.05165](#)].
- [25] A. Bogatskiy, B. Anderson, J.T. Offermann, M. Roussi, D.W. Miller and R. Kondor, *Lorentz Group Equivariant Neural Network for Particle Physics*, in *Proceedings of the International Conference on Machine Learning (ICML 2020)*, ICML, 6, 2020, DOI [[2006.04780](#)].
- [26] S. Gong, Q. Meng, J. Zhang, H. Qu, C. Li, S. Qian et al., *An efficient lorentz equivariant graph neural network for jet tagging*, *JHEP* **2022** (2022) 30.
- [27] A. Bogatskiy et al., *Symmetry Group Equivariant Architectures for Physics*, in *Snowmass 2021*, 3, 2022 [[2203.06153](#)].
- [28] J.T. Offermann, T. Hoffman and A. Bogatskiy, *Top Jet W-Momentum Reconstruction Dataset*, *Zenodo* **1.0.0** (2023) .
- [29] H. Weyl, *The Classical Groups. Their Invariants and Representations*, Princeton University Press, Princeton, N.J., 2 ed. (1946).
- [30] B. Gripaios, W. Haddadin and C.G. Lester, *Lorentz- and permutation-invariants of particles*, *J. Phys. A Math. Theor.* **54** (2021) 155201.
- [31] M. Zaheer, S. Kottur, S. Ravanbakhsh, B. Póczos, R.R. Salakhutdinov and A.J. Smola, *Deep Sets*, in *Adv. Neural Inf. Process.* 30, I. Guyon, U.V. Luxburg, S. Bengio, H. Wallach, R. Fergus, S. Vishwanathan et al., eds., pp. 3391–3401, Curran Associates, Inc. (2017), <http://papers.nips.cc/paper/6931-deep-sets.pdf>.
- [32] ATLAS collaboration, *Deep Sets based Neural Networks for Impact Parameter Flavour Tagging in ATLAS*, .
- [33] E. Wagstaff, F.B. Fuchs, M. Engelcke, M.A. Osborne and I. Posner, *Universal approximation of functions on sets*, *J. Mach. Learn. Res.* **23** (2022) Paper No. [151], 56.
- [34] G. Corso et al., *Principal neighbourhood aggregation for graph nets*, in *NeurIPS*, vol. 33, pp. 13260–13271, Curran, 2020, <https://proceedings.neurips.cc/paper/2020/file/99cad265a1768cc2dd013f0e740300ae-Paper.pdf>.
- [35] H. Pan and R. Kondor, *Permutation equivariant layers for higher order interactions*, in *AISTATS*, pp. 5987–6001, PMLR, 28–30 Mar, 2022, <https://proceedings.mlr.press/v151/pan22a.html>.
- [36] S. Villar, D.W. Hogg, K. Storey-Fisher, W. Yao and B. Blum-Smith, *Scalars are universal: Equivariant machine learning, structured like classical physics*, in *Adv. Neural Inf. Process.* 34, M. Ranzato, A. Beygelzimer, Y.N. Dauphin, P. Liang and J.W. Vaughan, eds., pp. 28848–28863, 2021, <https://proceedings.neurips.cc/paper/2021/hash/f1b0775946bc0329b35b823b86eeb5f5-Abstract.html>.
- [37] G. Kasieczka, T. Plehn, J. Thompson and M. Russel, *Top Quark Tagging Reference Dataset*, *Zenodo DataSet* **v0** (2018_03_27) (2019) .
- [38] DELPHES 3 collaboration, *DELPHES 3, A modular framework for fast simulation of a generic collider experiment*, *JHEP* **02** (2014) 057 [[1307.6346](#)].
- [39] I. Loshchilov and F. Hutter, *Decoupled weight decay regularization*, in *International Conference on Learning Representations*, 2019, <https://openreview.net/forum?id=Bkg6RiCqY7>.
- [40] J. Pearkes, W. Fedorko, A. Lister and C. Gay, *Jet Constituents for Deep Neural Network Based Top Quark Tagging*, [1704.02124](#).
- [41] H. Qu and L. Gouskos, *Jet tagging via particle clouds*, *Physical Review D* **101** (2020) .
- [42] M. Cacciari, G.P. Salam and G. Soyez, *FastJet User Manual*, *Eur. Phys. J. C* **72** (2012) 1896 [[1111.6097](#)].
- [43] D.E. Kaplan, K. Rehermann, M.D. Schwartz and B. Tweedie, *Top tagging: A method for identifying boosted hadronically decaying top quarks*, *Phys. Rev. Lett.* **101** (2008) 142001 [[0806.0848](#)].

A Additional results and plots

A.1 W-boson 4-momentum reconstruction

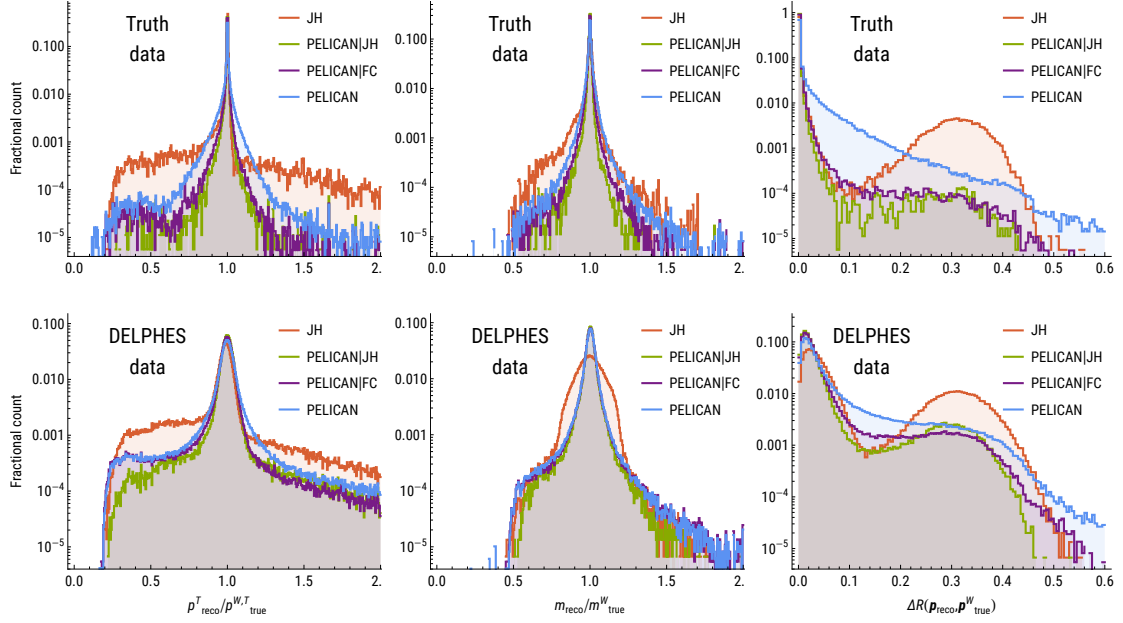


Figure 18: Full set of histograms corresponding to the entries in Table 3 (models trained targeting p_{true}^W , truth-level and DELPHES versions).

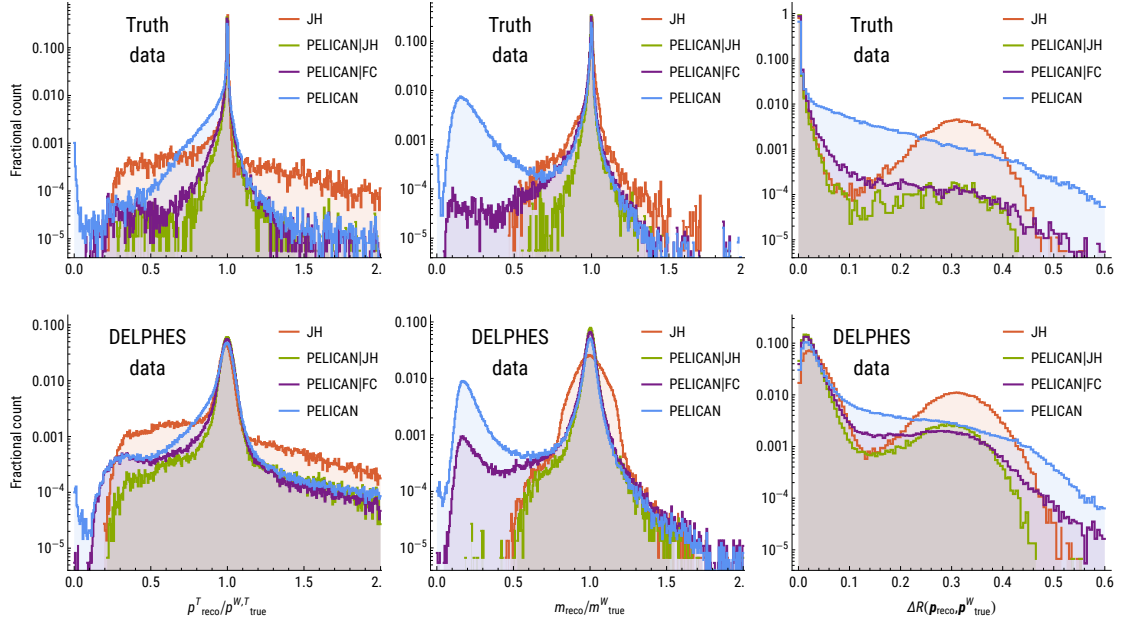


Figure 19: Full set of histograms corresponding to the entries in Table 4 (models trained targeting p_{cont}^W , truth-level and DELPHES versions, and compared to p_{true}^W).

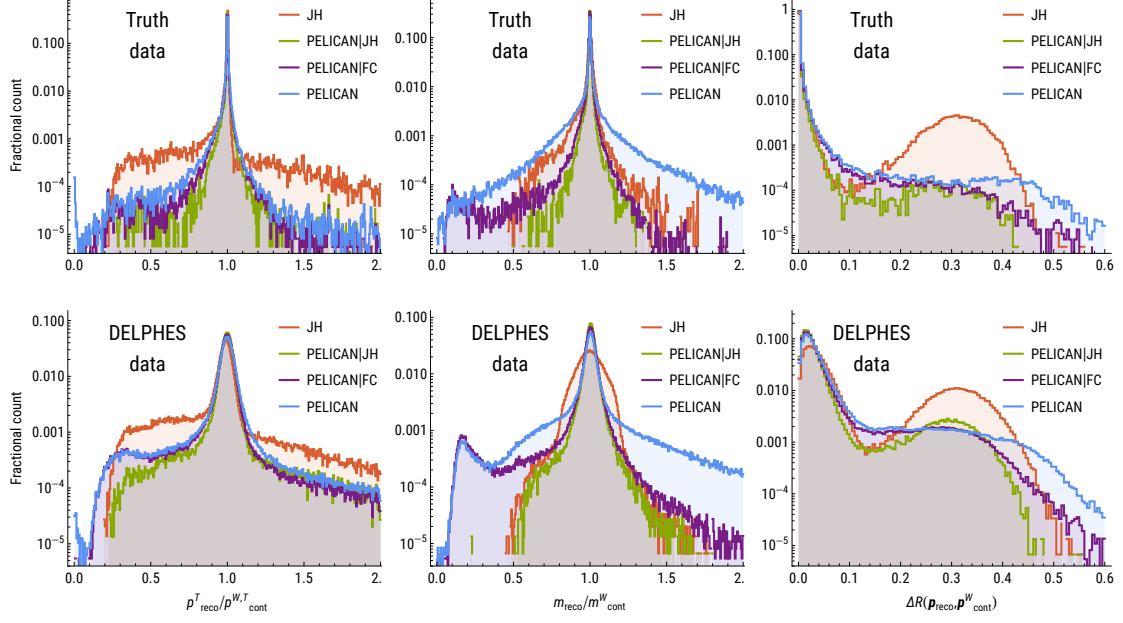


Figure 20: Full set of histograms for models trained targeting p_{cont}^W and compared to p_{cont}^W .

A.2 W-boson mass measurement

	Method	σ_{p^T} (%)	σ_m (%)	$\sigma_{\Delta R}$ (centirad)
Without DELPHES	JH	7.98%	4.75%	22.180
	PELICAN JH	0.26%	0.58%	0.111
	PELICAN FC	0.31%	0.76%	0.142
	PELICAN	0.88%	1.67%	0.548
With DELPHES	JH	16.0 %	12.0 %	25.4
	PELICAN JH	4.1 %	6.3 %	3.2
	PELICAN FC	4.7 %	7.3 %	3.5
	PELICAN	6.2 %	8.2 %	5.6

Table 7: PELICAN resolutions for models trained to reconstruct p_{true}^W with variable W mass.

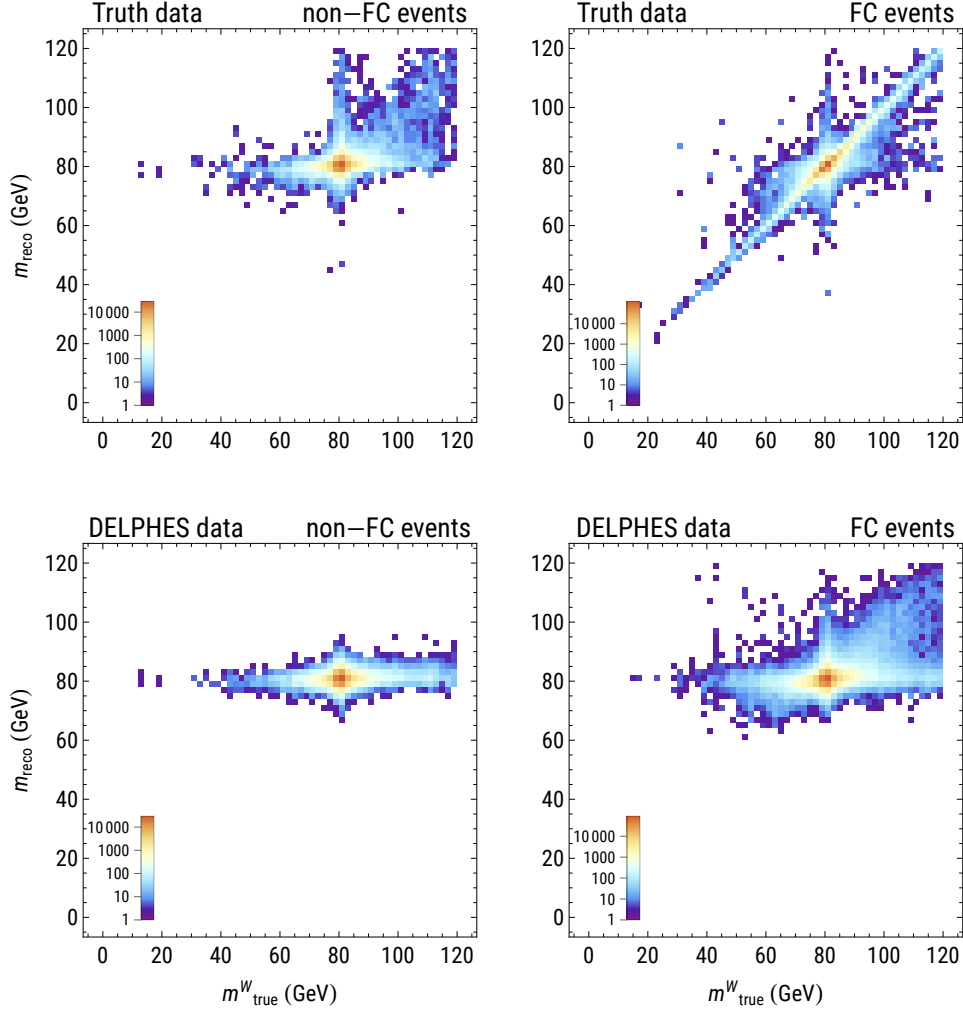


Figure 21: 2D histograms of target vs. reconstructed masses for models (top: truth data; bottom: `DELPHES` data) trained targeting p_{true}^W , broken up into two populations based on containment (left: non-FC events; right: FC events).

B IRC-safety and Lorentz symmetry

Let us now characterize the IRC-safe Lorentz invariants in the case of events consisting entirely of massless inputs (which is often artificially enforced in simulated data that includes detector simulations). When working with Lorentz-invariant observables, it is convenient to rewrite everything in terms of Lorentz invariant coordinates – the dot products $d_{ij} = p_i \cdot p_j$ (note that these coordinates are in general not independent since any 5×5 minor of the matrix $\{d_{ij}\}$ must vanish due to the fact that any five 4-vectors are linearly dependent, but they will suffice for our purposes). For two massless particles, collinearity is equivalent to the vanishing of the dot product. Conversely, the dot product between two time- or light-like vectors is zero only if both are light-like and collinear. Thus the C-safety condition amounts to the equality of the gradients of f with respect to any two of the rows (or columns) of $\{d_{ij}\}$ when evaluated on the corresponding coordinate hyperplane:

$$\left. \frac{\partial f}{\partial d_{ki}} \right|_{d_{ij}=0} = \left. \frac{\partial f}{\partial d_{kj}} \right|_{d_{ij}=0}. \quad (\text{B.1})$$

We intend to show that any smooth Lorentz-invariant observable f that is both IR-safe and C-safe in fact

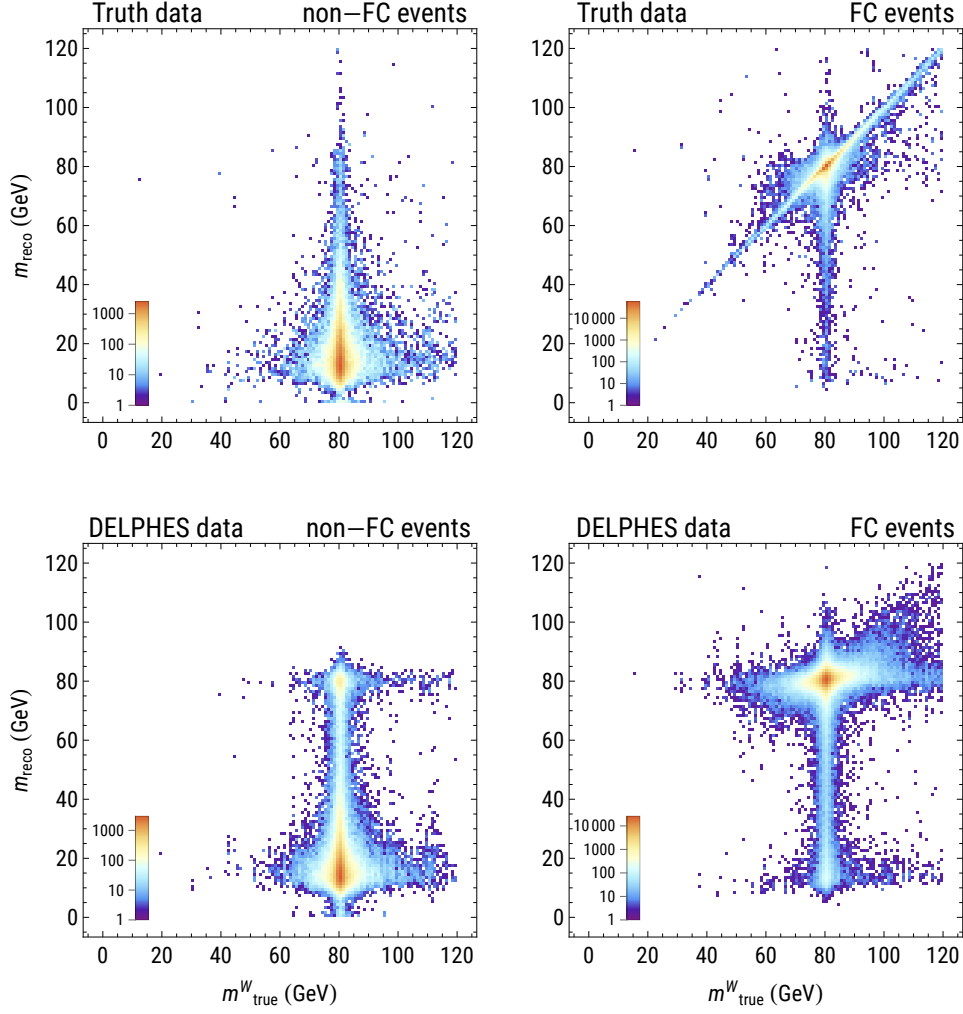


Figure 22: 2D histograms of true W mass vs. reconstructed contained mass for models (top: truth data; bottom: DELPHES data) trained targeting p_{cont}^W , broken up into two populations based on containment (left: non-FC events; right: FC events).

depends only on the jet mass $m_{\text{jet}}^2 = \sum_{k,l} d_{kl} = (\sum_k p_k)^2$. To that end, assume for a moment that this is not true. Then we can invoke IR-safety to summon a new input 4-vector $p_{N+1} = 0$ without changing the initial values of f , and then start varying it. Equation (B.1) must remain true for all values of the dot products $d_{i,N+1}$ and $d_{j,N+1}$. It is certainly impossible for both sides of the equation to be independent of $d_{i,N+1}$ unless f is independent of p_{N+1} , which would imply that f is a constant by permutation symmetry. If, as we assumed, f is functionally independent of m_{jet}^2 (i.e. $df \wedge dm_{\text{jet}}^2 \neq 0$), then due to permutation symmetry the partial derivatives with respect to *any* two different components of the matrix $\{d_{kl}\}$ do not always match, and the two sides of (B.1) will necessarily start diverging in value as we vary p_{N+1} , making f not C-safe. Therefore in the C-safe case the restriction to the coordinate hyperplane in (B.1) can be lifted so that the derivatives of f with respect to all dot products coincide, and hence f is only a function of m_{jet}^2 .

It is instructive to reflect on the interplay between IR-safety and C-safety. C-safety allows us to exchange momentum between collinear particles without affecting the values of C-safe observables, whereas IR-safety allows us to omit vanishing 4-momenta from the list of inputs. C-safety in itself doesn't change the number of input 4-vectors – it only requires f to be invariant under a certain transformation that mixes collinear massless inputs. Meanwhile IR-safety effectively requires f to encode an infinite family

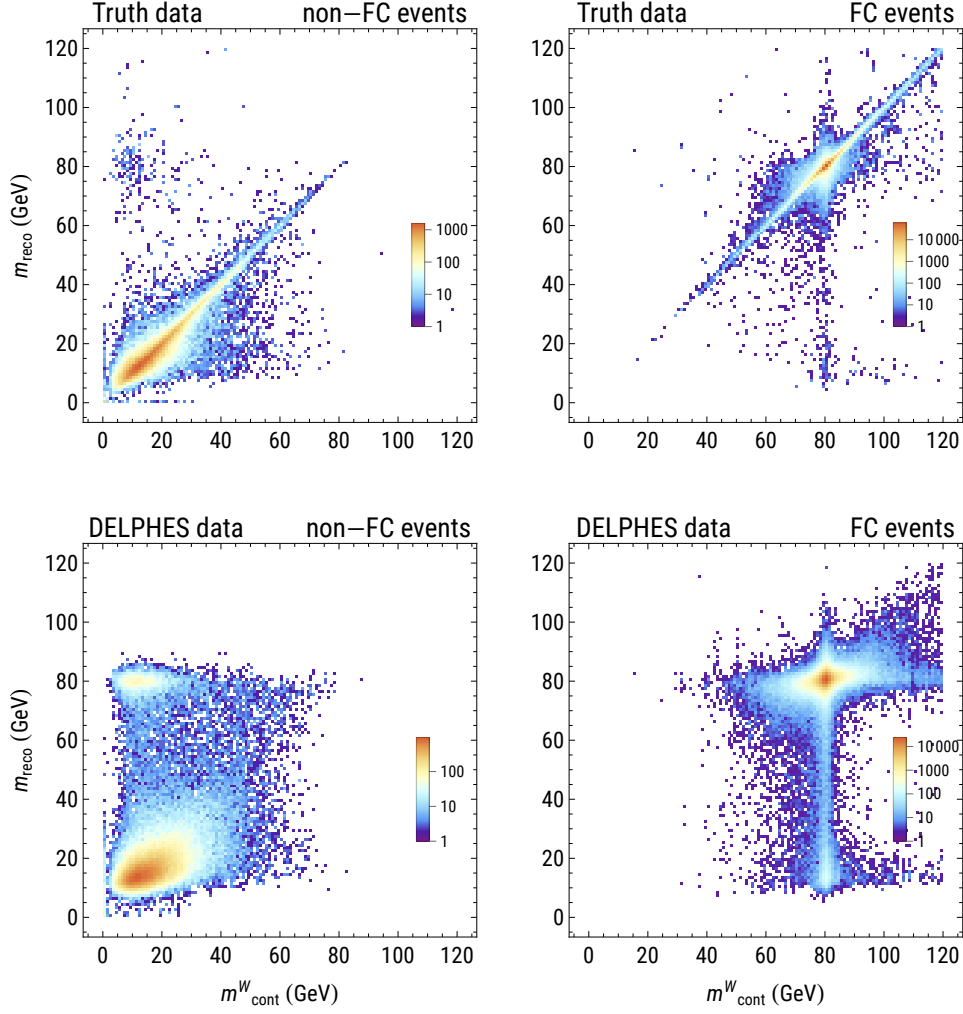


Figure 23: 2D histograms of target vs. reconstructed contained masses for models (top: truth data; bottom: DELPHES data) trained targeting p_{cont}^W , broken up into two populations based on containment (left: non-FC events; right: FC events).

of observables $f^{(N)}(p_1, \dots, p_N)$ for any possible number of inputs with the compatibility condition $f^{(N)}(p_1, \dots, p_{N-1}, 0) = f^{(N-1)}(p_1, \dots, p_{N-1})$. Only after combining C-safety with IR-safety do we arrive at the following result.

Theorem B.1. *An IRC-safe Lorentz-invariant observable with a mixture of massless and massive inputs can depend on the massless inputs only through their sum (which is generically a massive vector).*

In this way, IRC-safety is a significantly more powerful restriction than one could naively expect based on the definitions of IR and C-safety alone. As an example, consider the quantity $\prod_{i < j} d_{ij} = d_{12}d_{23}d_{31}$ on $N = 3$ massless inputs. It is in fact C-safe because it simply vanishes whenever any two inputs are collinear. However it is not IR-safe because sending $p_3 \rightarrow 0$ reduces the expression to zero instead of the expected d_{12} . Alternatively, as we will see in the following section, the natural IR-safe extension of $d_{12}d_{23}d_{31}$ to arbitrary N will not be C-safe.

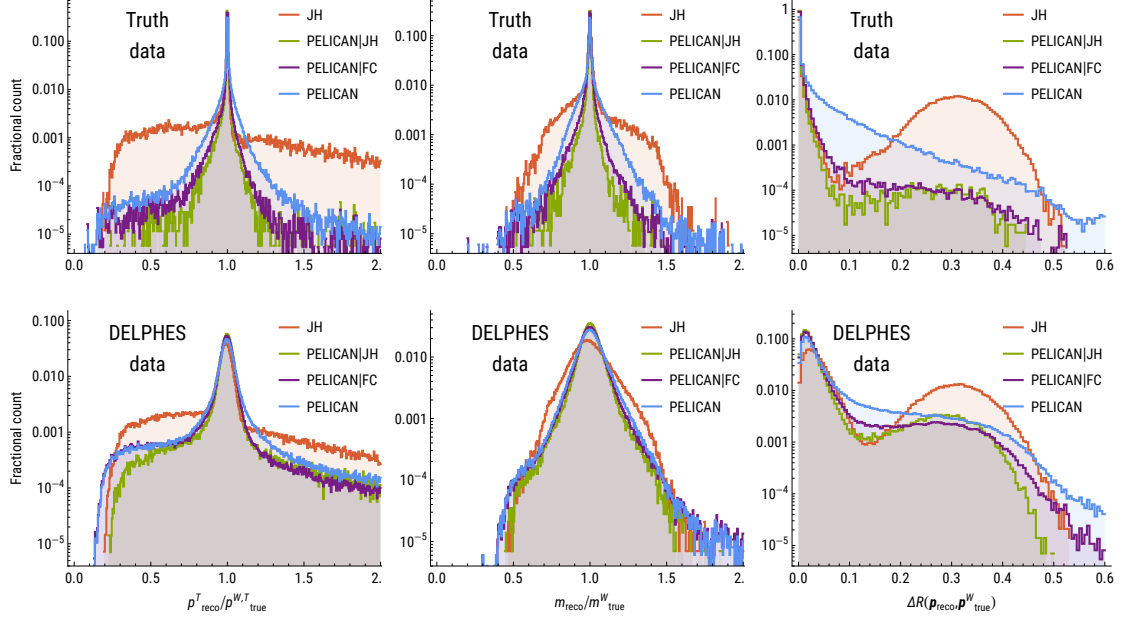


Figure 24: Full set of histograms corresponding to the entries in Table 7 (models trained targeting p_{true}^W , truth-level and DELPHES versions).

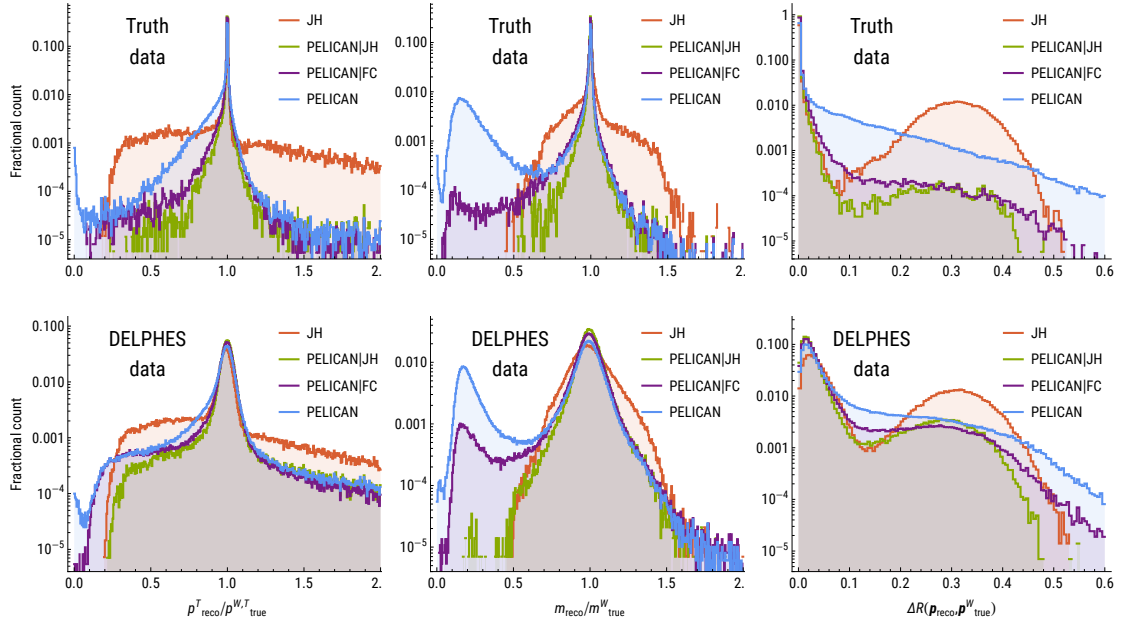


Figure 25: Full set of histograms corresponding to the entries in Table 5 (models trained targeting p_{cont}^W , truth-level and DELPHES versions, and compared to p_{true}^W).

B.1 Lorentz meets EFPs

Particle data is often analyzed via IRC-safe observables such as N -subjettiness [16]. A general polynomial basis for all IRC-safe observables was obtained in Ref. [18]. Here we first retrace some of the steps from the original derivation, and introduce a Lorentz-invariant analog at the end. Massless vectors can be written

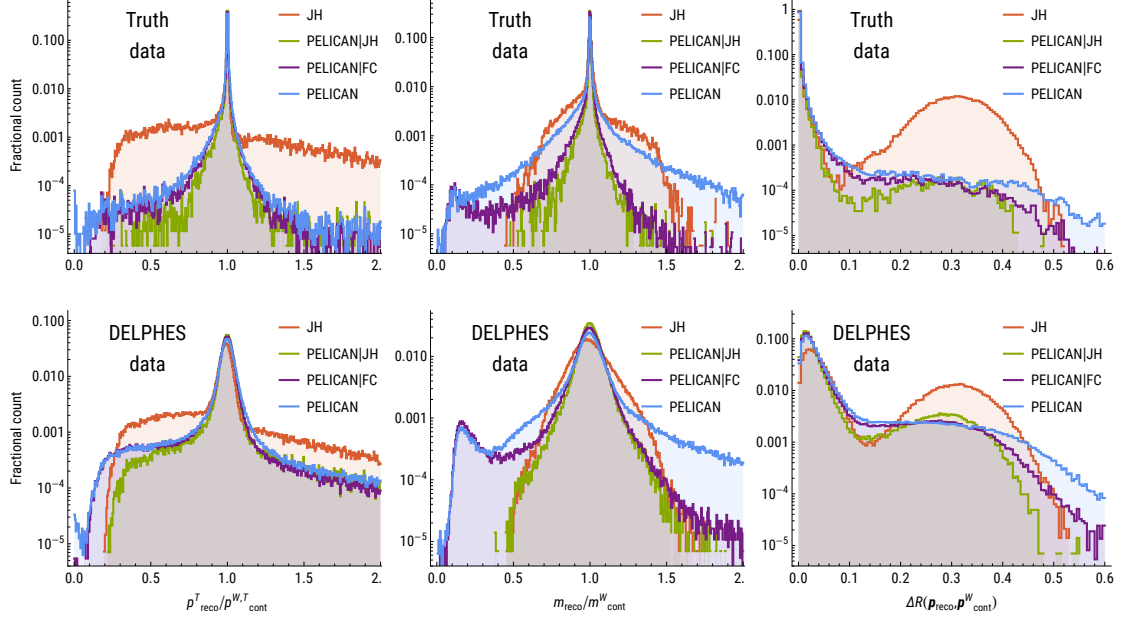


Figure 26: Full set of histograms for models trained targeting p_{cont}^W and compared to p_{cont}^W .

as $p = (E, E\hat{p})$ with a unit 3-vector \hat{p} . Then any (not necessarily Lorentz-invariant) smooth, symmetric observable of a set of N massless vectors can be expanded at low energies as a combination of terms (omitting the constant term) of the form

$$\sum_{i_1, \dots, i_M=1}^N \sum_{j_1, \dots, j_L=1}^N E_{i_1} \dots E_{i_M} \cdot f_{i_1, i_2, \dots, i_M}^{(N)}(\hat{p}_1, \dots, \hat{p}_N) \quad (\text{B.2})$$

with some “angular functions” $f_{i_1, i_2, \dots, i_M}^{(N)}$. As shown in Ref. [18], IR-safety for such a series amounts to requiring that the angular function $f_{i_1, i_2, \dots, i_M}^{(N)}$ in fact depends only on the particles whose indices are listed in the label of the function and is also independent of the total number N , i.e. it can be replaced by $f_{i_1, i_2, \dots, i_M}(\hat{p}_{i_1}, \dots, \hat{p}_{i_M})$. Furthermore, permutation symmetry of the entire observable descends to the total permutation symmetry of each angular function. Finally, C-safety requires that equating any two unit vectors $\hat{p}_i \rightarrow \hat{p}_j$ should lead to a function of only $E_1 + E_2$. At the level of angular functions, this implies that whenever i appears as an index in the subscript of the angular function, it can be replaced with j , and this can be done one index at a time. Ultimately this reduces the entire set of angular functions to just one $f_M = f_{1, 2, \dots, M}$, and therefore the order M term in the low-energy expansion of any IRC-safe observable becomes

$$\sum_{i_1, \dots, i_M=1}^N E_{i_1} \dots E_{i_M} \cdot f_M(\hat{p}_{i_1}, \dots, \hat{p}_{i_M}). \quad (\text{B.3})$$

From here, EFP’s are derived by expanding the angular functions into a Taylor series around small angles $\cos \theta_{ij} = \hat{p}_i \cdot \hat{p}_j$. The resulting polynomial expansion can be broken up into a linear basis enumerated by the set of isomorphism classes of multigraphs G with no loops (edges connecting a vertex to itself):

$$\text{EFP}_G = \sum_{i_1, \dots, i_M=1}^N \prod_{j \in V(G)} E_{i_j} \cdot \prod_{(k, l) \in E(G)} \theta_{i_k i_l}, \quad (\text{B.4})$$

where $V(G) = \{1, 2, \dots, M\}$ is the set of vertices of G , and $E(G)$ is the set of edges. The EFP is a homogenous polynomial in the energies of degree $|V(G)| = M$ and in the angles of degree $D = |E(G)|$. Notice that

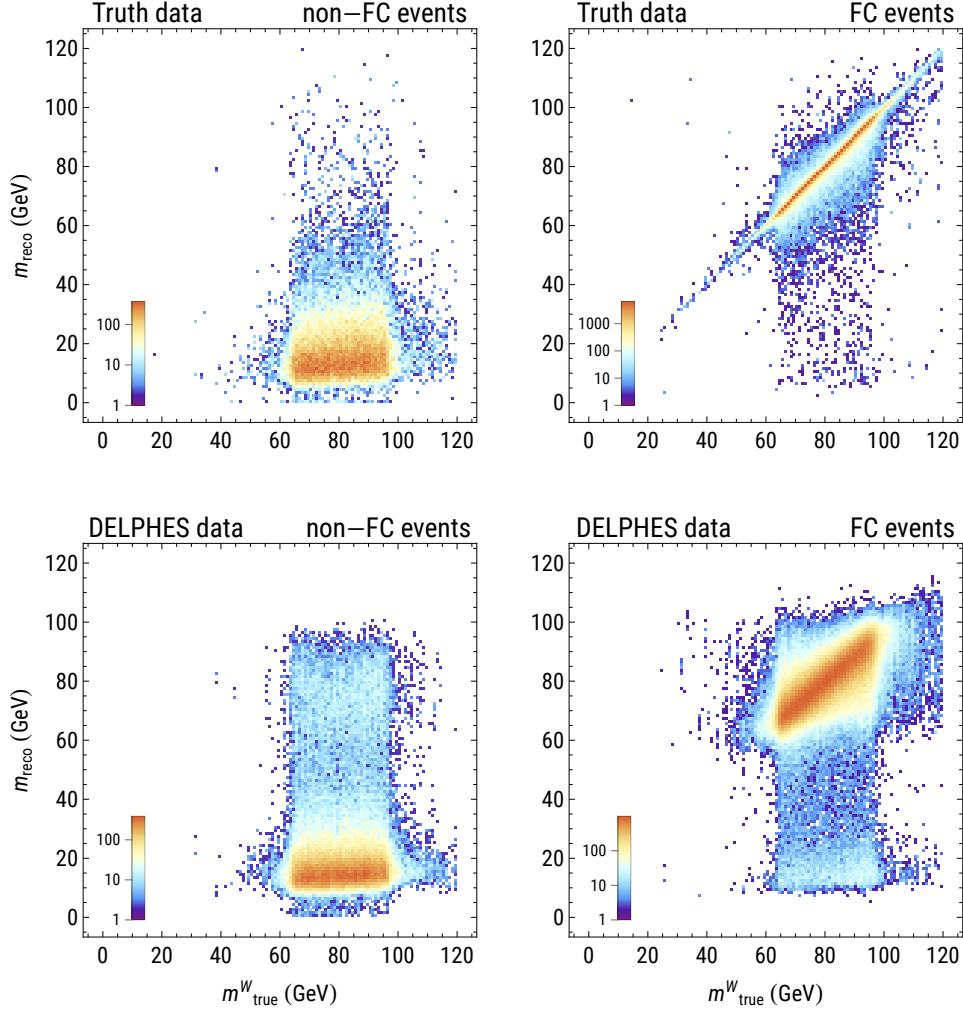


Figure 27: 2D histograms of target vs. reconstructed masses for models (top: truth data; bottom: DELPHES data) trained on the variable mass dataset targeting p_{cont}^W , broken up into two populations based on containment (left: non-FC events; right: FC events).

the indices i_j can coincide but the corresponding terms vanish since $\theta_{ii} = 0$, which is why multigraphs with loops are excluded from the basis. As a trivial but important example, the total energy $E = \sum_{i=1}^N E_i$ corresponds to $G = \bullet$. If G consists of multiple connected components, the resulting EFP is the product of the EFP's corresponding to the components, so the entire basis is algebraically generated by just the connected multigraphs.

It is instructive to see how IRC-safety works in EFP's. IR-safety is guaranteed by the mere presence of the energy pre-factors: sending $E_N \rightarrow 0$ will simply recover the same EFP for the remaining $N - 1$ particles. Meanwhile, C-safety is observed because if two particles, say 1 and 2, become collinear, then the angular factor is completely invariant under permutations of their two indices. In other words, all terms where the list (i_1, i_2, \dots, i_M) contains a fixed number, say L , of 1's or 2's, can be grouped together, and after summation over those indices the energy pre-factor manifestly depends on E_1 and E_2 only through an overall factor of $(E_1 + E_2)^L$. This is exactly the statement of C-safety.

Now let us task ourselves with identifying the subset of Lorentz-invariant IRC-safe observables. Obviously none of the EFP's are Lorentz-invariant due to the explicit dependence on angles, but smooth Lorentz-invariant observables can still be expanded in the EFP basis at small energies and angles. The only Lorentz-invariant of

two massless 4-vectors p_i, p_j is $p_i \cdot p_j = E_i E_j (1 - \cos \theta_{ij})$. At small angles the approximately boost-invariant combination is then $E_i E_j \theta_{ij}^2$. The expansion of any permutation-symmetric function of such dot products into a series as above will differ from general EFP's as follows: every angle θ_{ij} must appear in the product an even number of times, and the pre-factor must consist of nothing but one factor of $E_i E_j$ for every factor of θ_{ij}^2 . In each EFP only a subset of terms will generally satisfy this condition, so a better representation of the Lorentz-invariant basis is warranted.

Let us start again with the most general Lorentz-invariant and permutation-invariant observable of N 4-momenta. As we know, it is a function of only the dot products $d_{ij} = p_i \cdot p_j$. Such a function can be expanded at small arguments into terms like

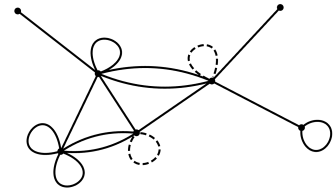
$$f_G^{(N)} = \sum'_{i_1, \dots, i_M=1}^N \prod_{(k,l) \in E(G)} d_{i_k i_l}, \quad (\text{B.5})$$

where the prime indicates that the terms where any two of the indices coincide are excluded. Including them would also produce a valid basis, but we leave them out to reduce the complexity of each polynomial. Such terms simply correspond to other multigraphs obtained from G by vertex identification, and those already appear in the expansion with independent coefficients. Unlike in EFP's, we also allow multigraphs with loops since we are not restricting ourselves to purely massless inputs. However, if all inputs are massless, all graphs with loops will produce vanishing polynomials.

Now we can easily see how to enforce IRC-safety in these polynomials. IR-safety requires that sending any of the 4-momenta to zero, say $p_N \rightarrow 0$, must be equivalent to simply restricting the same expression to only the other $N - 1$ particles. We observe that the only case when this is not already satisfied in the expression above is when the multigraph G contains isolated vertices (vertices of degree zero). Isolated vertices lead to summations over dummy indices corresponding to those vertices, which results in an overall factor of some power of N . The multiplicity N is not an IR-safe variable, and it is sufficient to ban graphs with isolated vertices to enforce IR-safety. We can thus drop the notation $f_G^{(N)}$ and simply write f_G with the implicit understanding that (B.5) defines the full infinite family of observables for all N .

Now we address C-safety. Much like in EFP's, C-safety in f_G 's means that whenever, say, p_1 and p_2 are massless, each monomial that contains a certain number of indices equal to 1 or 2 must match its coefficient with any other monomial that differs only by flipping any number of the indices from 2 to 1 or vice versa. In the language of multigraphs, this means that each monomial that assigns a vertex of degree n_1 to p_1 and another vertex of degree n_2 to p_2 must in fact result as just one among all possible monomials obtained via vertex identification from a graph G' where those two vertices have been “blown up” into $n_1 + n_2$ vertices of degree one. We also notice that this condition applies only to vertices that do not have any loops attached to them because otherwise the corresponding terms would vanish as p_1 and p_2 become massless, thereby making any additional restrictions unnecessary. To summarize, any IRC-safe polynomial contains with equal coefficients all f_G 's with G 's obtained by any combination of vertex identifications from some multigraph G' such that all of its loopless vertices are *leaves* (i.e. of degree one). We shall call such multigraphs *loop-saturated*. In this process it is sufficient to allow identifications of only the leaf vertices because all other vertex identifications will result in a polynomial independently defined by another loop-saturated multigraph.

Figure 28: The addition of the dashed loops makes this multigraph *loop-saturated*: all non-leaf vertices come with at least one loop. Loop-saturated multigraphs enumerate all IRC-safe polynomials.



We thus define an IRC-safe Lorentz-invariant polynomial basis indexed by non-isomorphic loop-saturated multigraphs G with no isolated vertices. Assuming the vertices of G are identified with the set $\{1, 2, \dots, M\}$, we write

$$\text{MFP}_G = \sum_{i_1, \dots, i_M=1}^N \prod_{(k,l) \in E(G)} d_{i_k i_l} \quad (\text{B.6})$$

where the sum is taken over all M -tuples, and an alternative basis

$$\text{MFP}'_G = \sum'_{i_1, \dots, i_M=1}^N \prod_{(k,l) \in E(G)} d_{i_k i_l}, \quad (\text{B.7})$$

where the coincidence of two or more indices $i_k = i_l$ is allowed only if their corresponding vertices (k and l) are leaves of G . MFP_G is simply MFP'_G plus a linear combination of certain MFP'_H 's with fewer vertices, namely such that H is a graph obtained from G by one or more vertex identifications each of which involves at least one non-leaf vertex of G . Indeed, such identifications preserve the property of being loop-saturated, and all other identifications are already included in the definition of MFP'_G .

Note that just like for EFP's, disconnected multigraphs correspond to products of their connected components (this holds for MFP_G but not for MFP'_G):

$$\text{MFP}_{G \sqcup H} = \text{MFP}_G \cdot \text{MFP}_H. \quad (\text{B.8})$$

As an example, if all inputs are known to be massless, then any connected multigraph with loops will produce a vanishing polynomial. And the only loopless loop-saturated connected multigraph is the graph consisting of just one edge, which evaluates to the jet mass: $\text{MFP}_{\bullet-\bullet} = \sum_{i,j} d_{ij} = m_{\text{jet}}^2$. Therefore in the massless case we generate all analytic functions of m_{jet}^2 , which is exactly what we expect based on the results of the previous section. Lastly, returning to the example from the last section, $d_{12}d_{23}d_{31}$, it can only be interpreted as an IR-safe polynomial if it corresponds to the triangle graph. However, such a graph is not loop-saturated, and therefore this polynomial is not IRC-safe despite being C-safe for $N = 3$ (which can be confirmed by observing that for $N = 4$ the triangle graph generates a non-C-safe polynomial), and the correct IRC-safe completion is simply m_{jet}^6 .

B.2 Quantifying IRC-safety

Let $f^{(N)}$ be a Lorentz-invariant permutation-symmetric observable defined for varying number N of inputs, for instance the output of a PELICAN instance. We define the following difference operator that measures the obstruction to f being IR-safe:

$$\Delta^{\text{IR}} f^{(N)} = f^{(N+1)}(p_1, \dots, p_N, 0) - f^{(N)}(p_1, \dots, p_N). \quad (\text{B.9})$$

IR-safety is equivalent to the vanishing of this operator:

$$\text{IR - safety : } \Delta^{\text{IR}} f = 0. \quad (\text{B.10})$$

Furthermore, we can define *IR-robustness* as the partial derivative corresponding to the injection of an infinitesimally soft but non-zero 4-momentum:

$$\text{IR - robustness : } R_p^{\text{IR}} f^{(N)} = \frac{d}{d\epsilon} \epsilon = 0 f^{(N+1)}(p_1, \dots, p_N, \epsilon p). \quad (\text{B.11})$$

All together, we have the following series expansion for a general observable near $p_{N+1} = 0$:

$$f^{(N+1)} = f^{(N)} + \Delta^{\text{IR}} f^{(N)} + \left(R_{p_{N+1}}^{\text{IR}} f^{(N)} \right) \cdot p_{N+1} + \mathcal{O}(p_{N+1}^2). \quad (\text{B.12})$$

An IR-safe observable must always have $\Delta^{\text{IR}} f = 0$, and lower values of IR-robustness indicate lower sensitivity to soft particles. In practice, we can evaluate the ratio $(\Delta^{\text{IR}} f^{(N)})/f^{(N)}$ and average it over a testing dataset to quantify the IR-safety of PELICAN.

For C-safety, we pick a massless 4-vector p and define the differential operator

$$D_p^{\text{C}} f = \frac{d}{d\lambda} \lambda = 0 f(p_1 + \lambda p, p_2 - \lambda p, p_3, \dots). \quad (\text{B.13})$$

C-safety then is equivalent to the requirement that $D_p^{\text{C}} f = 0$ for any massless p whenever p_1 and p_2 are collinear with p :

$$\text{C - safety : } D_p^{\text{C}} f|_{p_1 \parallel p_2 \parallel p} = 0, \quad p^2 = 0. \quad (\text{B.14})$$

C-robustness can be easily defined as the second-order analog of D_p^C . Namely, we pick a second vector \hat{p} such that $p \cdot \hat{p} = 0$ (which means that \hat{p} is tangent to the light cone at p) and measure how quickly $D_p^C f$ deviates from zero as we deform p_1 and p_2 away from collinearity:

$$\text{C-robustness : } R_{\hat{p},p}^C f = D_{\hat{p}}^C D_p^C f, \quad \hat{p} \cdot p = p^2 = 0, \quad p_1 \parallel p_2 \parallel p. \quad (\text{B.15})$$

It is instructive to express these quantities in terms of the dot products d_{ij} . We have

$$D_p^C f = \sum_{j=1}^N (\partial_{1j} f - \partial_{2j} f) (p_j \cdot p), \quad (\text{B.16})$$

where ∂_{kl} indicates the partial derivative with respect to d_{kl} . Note that individual partial derivatives aren't really well-defined due to the fact that $\{d_{ij}\}$ is not a set of independent coordinates on the manifold of N 4-vectors for $N \geq 5$. However, combinations such as above are valid since they are nothing but a different way of expressing the original well-defined operator. We also immediately notice that if $N = 2$ and $p_1 \parallel p_2 \parallel p$, then $D_p^C f = 0$ automatically. Indeed, every Lorentz-invariant observable for two particles is *C*-safe due to the fact that $d_{12} = \frac{1}{2}(p_1 + p_2)^2$ for massless inputs.

C-robustness is similarly expressed by

$$R_{\hat{p},p}^C f = \sum_{i,j=1}^N \left(\partial_{1i,1j}^2 + \partial_{2i,2j}^2 - \partial_{1i,2j}^2 - \partial_{1j,2i}^2 \right) f \cdot (p_i \cdot \hat{p})(p_j \cdot p). \quad (\text{B.17})$$